

Tree Tensor Network ansatz in 1D & 2D

MSc Thesis (*Afstudeerscriptie*)

written by

Ruben Timmermans.

(born September 27th, 1992 in Haarlem, the Netherlands)

under the supervision of **Dr Philippe Corboz**, and submitted to the
Board of Examiners in partial fulfillment of the requirements for the degree
of

MSc in Theoretical Physics

at the *Universiteit van Amsterdam*.

Abstract

In this thesis the Tree Tensor Network ansatz is explained along with a study of its capabilities when applied to both the 1D and 2D Transverse Field Ising model, and the 2D $J_1 - J_2$ Heisenberg model on finite systems. It is shown that the Tree Tensor Network ansatz can produce accurate results within the range of system sizes that also allow for a comparison to the exact diagonalization results. In addition the results for the J_1 - J_2 Heisenberg model are compared to results in the literature.

Contents

1	Introduction	3
2	Introduction to Tensor Networks	5
2.1	Introduction	5
2.2	Entangled- and Product-states	6
2.3	Diagrammatic notation	6
2.3.1	Multiplication and Reshaping of Tensors	7
2.4	Matrix product states	9
2.4.1	Schmidt and singular value decomposition	10
2.4.2	Reduced density matrix formalism	12
2.4.3	Entropy and Area law	12
2.4.4	Canonicity	14
2.4.5	Computation of expectation values	15
2.4.6	Simple optimisation	15
3	Tree Tensor Network Ansatz	18
3.1	Introduction	18
3.2	Tree Tensor Network Ansatz	19
3.2.1	Isometries	19
3.2.2	Canonical form	21
3.3	Computation of Operators	22
3.3.1	one- and two-site operators	22
3.3.2	Reduced density matrix	23
3.3.3	Relation to MERA	25
3.3.4	Implementing symmetries	25
4	Methods	26
4.1	Introduction	26
4.2	Optimisation strategy	27

4.2.1	Cost-function	27
4.2.2	Optimisation of an isometry	28
4.2.3	Cost of optimisation	29
5	Models	33
5.1	Introduction	33
5.2	Transverse field Ising model	33
5.3	Heisenberg J_1-J_2 model	36
5.3.1	Introduction	36
6	Results & discussion	46
6.1	Introduction	46
6.2	Transverse Field Ising: 1D	47
6.2.1	Ground-state energy	47
6.2.2	Magnetization	50
6.2.3	Entanglement entropy	50
6.2.4	Correlation functions	52
6.2.5	Iteration time scaling and convergence	54
6.3	Transverse Field Ising: 2D	56
6.3.1	Ground-state energy	56
6.3.2	Magnetization	59
6.3.3	Entanglement entropy	60
6.3.4	Correlation functions	61
6.3.5	Iteration time scaling and convergence	62
6.4	J_1-J_2 Heisenberg model	65
6.4.1	Ground-state energies	65
6.4.2	Entanglement entropy	68
6.4.3	Correlation functions	69
7	Conclusion & outlook	74
8	Acknowledgements	76
Appendix A	Details about Code	77
A.1	Introduction	77

Chapter 1

Introduction

Solving Quantum many-body problems by finding the ground-states, is of great importance in Condensed matter physics to study and explain exotic behaviours these problems can give rise to. They, however, are challenging to solve since a lot of these do not have exact solutions in order to gain insight on the underlying physics, yet numerous computational methods have been successful in solving these problems numerically, for example by means of an exact diagonalization. However, due to the exponentially growing Hilbert space this quickly becomes a practical problem due to the limitations on computing power. Therefore Quantum Monte Carlo methods, which are essentially Classical Monte Carlo methods in $d + 1$ dimensions, have been proposed to lower these costs whilst still giving accurate approximations to solutions of the original problem. However, due to the negative sign problem these simulations can only be done for bosonic and unfrustrated systems. Aside the Monte Carlo methods, another group of methods, referred to as *Tensor Network Methods* have been more successful mainly by eliminating the former problem [55, 39, 10, 12, 13].

In this thesis the capabilities of the binary Tree Tensor Network ansatz [47] are studied and its efficiency to produce accurate results for both the Transverse Field Ising, and the J_1 - J_2 Heisenberg model applied to 1D and 2D, and 2D systems respectively. First the models with their phases diagrams are explained where for the J_1 - J_2 model a more elaborate description is given considering the nature of the phase diagram around $J_1 = 2J_2$ is still under debate.

The thesis is organized up as follows: First the basics for TN methods are explained in chapter 2 followed by an example called *Matrix Product States* and a simple optimisation algorithm. Then the TTN is explained in chapter

3 and a gauge for the simulations is chosen after which the optimisation-strategy and models are explained in chapters 4 and 5 respectively. The results are shown in chapter 6 and further discussed in chapter 7.

Chapter 2

Introduction to Tensor Networks

2.1 Introduction

Tensor Network algorithms have been originally developed to study and simulate systems from the condensed matter physics field of research. However, in recent decades they have become increasingly popular in other fields of research (within physics) such as *statistical physics* [38, 30, 19, 14], *cosmology* and *quantum gravity* [45, 3, 8, 2, 36], *quantum chemistry* [56, 6, 46, 27], *quantum field theory* [48, 20], and even in the *artificial intelligence* field [35, 7, 32, 31, 17]. Most of these studies have been inspired by the invention Whites' *Density Matrix Renormalization Group* algorithm [55] which to date is still one of the most powerful tools for studying *1D* systems yet it was not seen as a tensor network tool until it was used in the context of *Matrix Product States* (MPS)[39].

Before we look further into the simplest ansatz, namely the MPS, I must emphasise an important problem of finding ground states for lattices in general. One of the main reasons that makes finding ground-states of quantum systems difficult is the exponential growth of the Hilbert space as a function of the system size. Consider the following example: Let us assume the we have a lattice consisting of N sites of simple spin $\frac{1}{2}$ particles thus leading to a local Hilbert space, H_i , of dimension $d = 2$. Every site is hence described by the basis $\{|\uparrow\rangle, |\downarrow\rangle\}$. Then the total Hilbert space is described by the direct product of these local Hilbert spaces, $H_{total} = H_1 \otimes H_2 \otimes \dots \otimes H_N$, which scales as d^N . This implies that to effectively describe any state in the total Hilbert space 2^N parameters are required, where $N = l$, $N = l \times l$ in *1D*

and $2D$ respectively. This clearly forms a problem as soon as N increases. Lastly, consider a state, $|\Psi\rangle$ in the former total Hilbert space decomposed into a tensor product of the local Hilbert spaces:

$$|\Psi\rangle = \sum_{i_1 i_2 \dots i_N} \Psi_{i_1 i_2 \dots i_N} |i_1 \otimes i_2 \otimes \dots \otimes i_n\rangle \quad (2.1)$$

The general focus of current day Tensor Network ansatzes is to accurately approximate the expansion components $\Psi_{i_1 i_2 \dots i_N}$ whilst not using the total Hilbert space of $|\Psi\rangle$ by means of a truncation of the Hilbert space which reduces the total amount parameters needed.

2.2 Entangled- and Product-states

Whenever a state can be described by a product of *vectors* e.g. $\Psi_{12\dots N} = \psi_1 \psi_2 \dots \psi_N$ this is referred to as a product state. However, usually quantum states cannot be described by a product of states especially at critical points (at phase transitions) of a given Hamiltonian since they are highly *entangled* meaning that its sub-states typically consists of a sum of basis states, e.g. $|\psi\rangle = \frac{1}{\sqrt{2}}(|\uparrow\downarrow\rangle - |\downarrow\uparrow\rangle)$, which can not be expressed as a product-state. In order to deal with these entangled states one can decompose Ψ into a product of *tensors*, e.g. $\Psi_{i_1 i_2 \dots i_n} \approx T_{i_1} T_{i_2} \dots T_{i_n}$ in order to approximate the expansion coefficients $\Psi_{i_1 i_2 \dots i_n}$ and represent the state. Further explanation of how one decomposes states such as $|\Psi\rangle$ into a network of tensors will be given in section 2.4. First the diagrammatic notation is explained in the next section, 2.3

2.3 Diagrammatic notation

A tensor can be thought of as a generalisation of a n dimensional array where the entries usually have complex values and the tensors can also have different symmetries incorporated in them. The rank of a tensor is a classification of the amount of dimensions it lives in. For instance, a vector v^i is referred to as a rank $(1, 0)$, whereas its dual form v_i is referred to as rank $(0, 1)$ tensor. In general a rank (n, m) tensor has the following form.

$$A_{J_1 \dots J_m}^{i_1 \dots i_n} \quad (2.2)$$

However, usually in the context of Tensor Network no distinction between lower and upper indices is made unless stated explicitly. The terms *rank*,

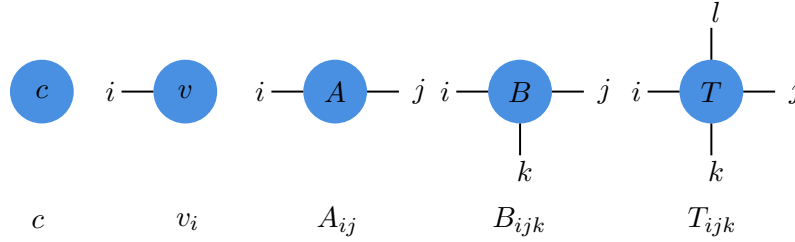


Figure 2.1: examples of different types of tensors in the diagrammatic notation

order, *valence*, and *degree* are also often used interchangeably though imply the same, namely the dimension of the tensor. In this thesis the total number of indices of a tensor will be referred to as *rank* for the sake of both clarity as consistency.

Since tensor networks typically consists of many tensors and therefore also many indices, expressions of these networks can get very complex and lengthy. Therefore the diagrammatic notation is a very useful tool to reduce the seemingly complex nature of these networks by representing tensor objects by a shape depending on their properties, and indices by lines. As illustrated in figure 2.1, tensors are represented as a circular shape and their indices, also referred to as *legs*, are represented by open lines. For examples of tensors of different *ranks* see figure 2.1.

2.3.1 Multiplication and Reshaping of Tensors

When a tensor network is contracted the lines connecting the tensors are the axis to be contracted over and the open lines are the axis not contracted over. The dimension of the closed lines are often referred to as the *bond dimension* whereas the open lines are often referred to as *legs* or *physical legs*. Using this concept one can view complicated networks and even simple networks such as a *matrix vector* product in the diagrammatic notation, see 2.2 for examples.

Since tensor networks usually consists of a lot of tensor instead of maximally 3 like in 2.2 one needs to take into account the significance of the order in which a network is contracted. If one for instance wants to perform the multiplication of:

$$\sum_{ijk} A_{ikl} B_{ijk} C_{jkmn} = D_{lmn} \quad (2.3)$$

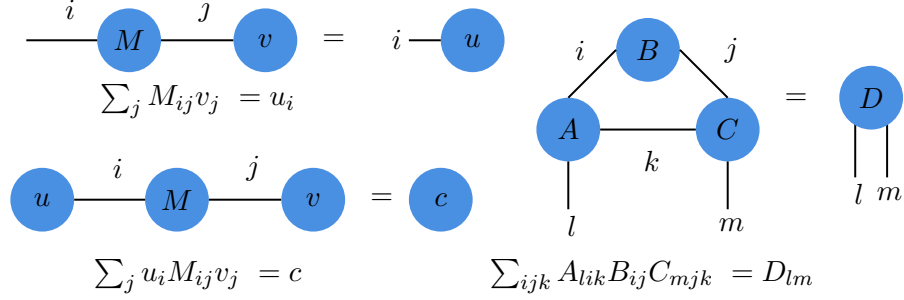


Figure 2.2: Examples of contractions for different types of tensors

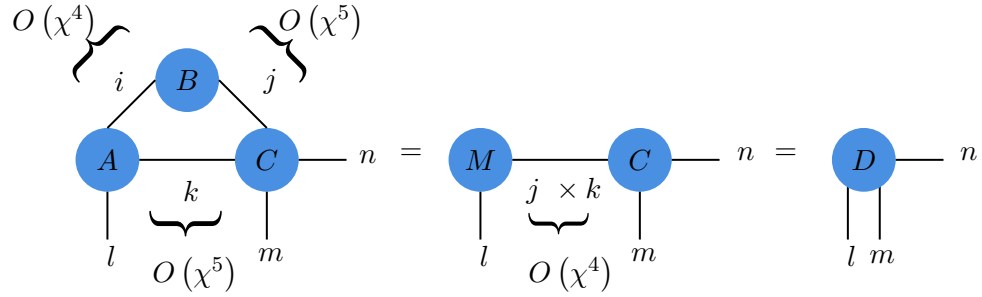


Figure 2.3: Cost of contraction of equation 2.3.

represented by contracting the network in figure 2.3, multiple orderings of contractions are possible. The cost of a specific order is computed by looking at the *legs* involved in the contraction of the concerned tensors, more specifically one needs to multiply these resulting dimensions to get the total order of the contraction. In this example first contracting A_{lik} with B_{ijk} first leads to the lowest cost if we assume that:

$$\dim(i) = \dim(j) = \dim(k) = \dim(l) = \dim(m) = \dim(n) = \chi$$

since $\dim(i) \times \dim(k) \times \dim(k) \times \dim(l) = O(\chi^4)$. As already seen in the contraction order example in 2.3, sets of legs can either be reshaped into a smaller set of legs or split into a larger set of legs. For a concrete example see figure 2.4

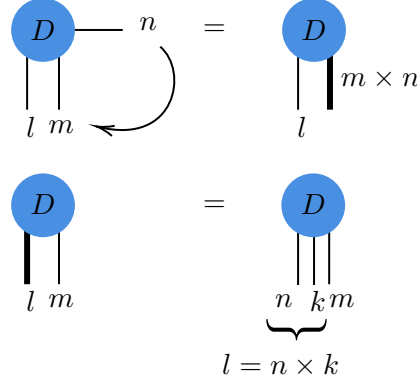


Figure 2.4: Examples of reshaping tensors.

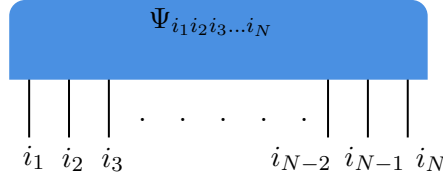


Figure 2.5: Diagrammatic representation of the full state $\Psi_{i_1 i_2 i_3 \dots i_N}$

2.4 Matrix product states

The first tensor network ansatz established for 1 dimensional systems is the *Matrix Product State* or abbreviated *MPS* and is based on White's DMRG proposal, as is its generalisation to 2 dimensional systems the *Snake Matrix Product State*, *sMPS*. Although the TTN ansatz in this thesis differs from both the MPS as the sMPS in the sense that the TTN is more related to RG as it inherently coarse grains *real space*, the MPS and sMPS are useful to serve as examples and explain the basic concepts of tensor networks for finite systems. Therefore in this section the basics of tensor networks will be explained such that section 3 on the TTN is more understandable.

Let us recall the state introduced in equation 2.1 whose diagrammatic notation is illustrated in figure 2.5. The idea behind the MPS is to instead of viewing the state from 2.1 as one tensor with N physical leg, first decomposing the state and then like the name suggest, view the state as a product of tensors as illustrated in figure 2.6 which can be done by iteratively applying a singular value decomposition on a partition of the state, the latter is explained in the next section. Notice that the cost of representing the state

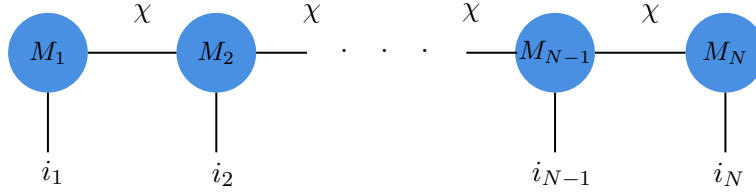


Figure 2.6: Decomposition of $\Psi_{i_1 i_2 i_3 \dots i_N}$ into $M_{i_1} M_{i_2} \dots M_{i_{N-1}} M_{i_N}$

of figure 2.5 scales exponentially in N , d^N (product of local Hilbert spaces), whereas the cost of representing the state in figure 2.6 merely scales polynomially in N , χ^N . This is already a significant reduction in computational costs for working with these networks. The *bond dimension* χ , can be tuned even further leading to even larger computational savings in terms of costs. Since most random states in Hilbert space are highly entangled, having a finite bond-dimension in a tensor network will fail to accurately describe the corresponding states. However, the states of interest in this thesis are ground-states of local Hamiltonians, which are typically less entangled than random states and can therefore be effectively described by means of a tensor network.

In the following subsections the motivation for this decomposition and the methods on how to decompose a general state Ψ in the form of figure 2.6 are explained.

2.4.1 Schmidt and singular value decomposition

Instead of decomposing Ψ into a chain of tensors one can also simply decompose a state into two bi-partitions - halves - of the system, namely A and B , both with their own local Hilbert spaces H_A and H_B such that $H_{total} = H_A \otimes H_B$. Recall that any wave function can be decomposed into an orthonormal basis $|i\rangle$ and $|j\rangle$ as follows

$$|\Psi\rangle = \sum_{ij}^n \Psi_{ij} |i\rangle |j\rangle \quad (2.4)$$

The *Schmidt* decomposition is an alternate form of decomposing the state Ψ , where the Ψ is decomposed according to:

$$|\Psi\rangle = \sum_i^n S_i |a_i\rangle |b_i\rangle \quad (2.5)$$

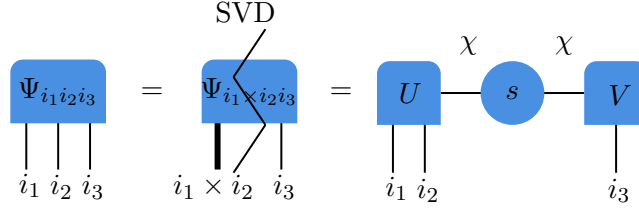


Figure 2.7: Singular value decomposition on a state

Where S_i are called singular values and obtained via the *singular value decomposition* of Ψ after having reshaped the state *vector* into a *matrix* form of size $i \times i$. A singular value decomposition (SVD) expresses any matrix M into two unitary matrices U and V along with a diagonal matrix containing the singular values which have $\|S_i\| > 0 \forall i$ and the number of singular values is referred to as the *Schmidt rank* or *Schmidt number*.

$$\Psi_{ij} = \sum_l U_{il} s_l V_{jl}^\dagger \quad (2.6)$$

which when inserted into equation 2.4 results into equation 2.5 after a simple basis transformation. Notice that the SVD is in fact a generalisation of the *eigenvalue decomposition* (sometimes called *spectral decomposition*) to non-square matrices ($n \times m$) since:

$$\begin{aligned} \Psi^\dagger \Psi &= (U s V^\dagger) (U s V^\dagger) \\ &= V s U^\dagger U s V^\dagger \\ &= V s^2 V^\dagger \end{aligned}$$

the SVD will prove to be very useful when working with tensor networks. For a visual example of a simple SVD procedure see figure 2.7.

Interesting to mention is how one can identify entangled or product states in this decomposition. More specifically, when is a state entangled? Let us recall what is mentioned in section 2.2, a state is separable or not entangled when it can be expressed as a product state, $|\psi\rangle = |\phi_1\rangle \otimes |\phi_2\rangle$. This is easily read off the singular values in the Schmidt decomposition. If all singular values but one singular value are 0 then the state is simply a product state and the state is not entangled. In the other extreme case contrary to the product state, when the state has singular values that are equal in magnitude and not zero and follow a flat distribution $\frac{1}{\sqrt{N}}$, then the state is called *maximally entangled*.

In general the amount of basis states needed (χ) to describe a wave function is equal to the Schmidt rank, which for product states is 1 and can maximally be N . Although for maximally entangled state the bond dimension χ to accurately describe a wave function can become very large, the decay of the singular values spectrum usually is very rapid, implying that not all singular values need to be kept in order to faithfully represent a state. The idea behind current DMRG techniques is that one tries to find a bond dimension for $\chi \ll N$ by keeping every state in the decomposition up to χ and disregarding others, and also minimising the error between the *exact state* $|\Psi\rangle$ and the approximated state $|\tilde{\Psi}\rangle$ during the optimisation of the tensor network created by a decomposition of the state into a certain ansatz.

2.4.2 Reduced density matrix formalism

The density matrix formalism is essential in DMRG, since it is originally based on the density matrix. Let us start by introducing the most general form of a density matrix (*density operator*).

$$\rho = \sum_i p_i |\psi_i\rangle \langle \psi_i| \quad (2.7)$$

Where $\|p_i\| > 1$ are the eigenvalues of ρ and $\sum_i p_i = 1$. When the state is *pure* the density matrix has only 1 eigenvalue that is non zero and hence equal to 1 and therefore reduces to a single outer product, $\rho = |\Psi\rangle \langle \Psi|$. However, when the state is *mixed* the density matrix can merely be expressed as in equation 2.7. Using this definition for the reduced density matrix one can also define a *reduced density matrix* which is obtained by *tracing* out the part of the state one is not interested in e.g. :

$$\rho_A = \text{Tr}_B (\rho_{AB}) = \sum_i \langle b_i | \Psi \rangle \langle \Psi | b_i \rangle = \sum_i p_i |a_i\rangle \langle a_i| \quad (2.8)$$

Where, in fact, the p_i correspond to the singular values square (S_i^2). In figure 2.8 the diagrammatic form is given for the procedure of constructing a reduced density matrix for the simplest case.

2.4.3 Entropy and Area law

With the definitions of pure states, mixed states, and the reduced density matrix one can define obtain the *von Neumann entropy* which serves as a measure of entanglement.

$$S = -\rho \log \rho = \sum_i p_i \log p_i \quad (2.9)$$

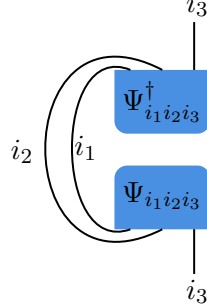


Figure 2.8: Example of the reduced density matrix of i_3 : $\rho_{i_3} = \text{Tr}_{i_1 i_2} (\Psi_{i_1 i_2 i_3})$

Usually one is interested in the entanglement entropy between partitions of the state and one can define an entanglement entropy on that partition by tracing out the environment as follows:

$$S_A = -\text{Tr}_B (\rho \log \rho) = -\rho_A \log \rho_A = \sum_{\alpha} p_{\alpha} \log p_{\alpha} \quad (2.10)$$

Where p_i and p_{α} are the eigenvalues of the density matrices. A product state yields an entropy, S_A of 0 since $p_1 = 1$ and all other p_i are zero hence $-1 \log 1 = 0$. Whereas for a maximally entangled state the eigenvalues are given by a flat distribution $1/M$, M being the number of eigenvalues, and yield a $S_A = \log M$. Given the bipartition of a the system one can ask how the entropy depends on the system size L . Since a random state in Hilbert space is generally not a product state, let alone a pure state, most of the p_i do not vanish and need to be kept which results in an entanglement entropy that scales with L , $S_A \sim L^d$, d being the dimension of the system. However, studies [4], [43] have shown that ground-states of local Hamiltonians typically not scale with the volume of the system but with its area and obey an entropic area law

$$S_A = L^{d-1} \quad (2.11)$$

S Since for local Hamiltonians the interacting boundary is where most of the entanglement between A and B is stored. Furthermore, for 1 dimensional systems $d = 1$, it is proven that the entanglement entropy stays constant for every L [21], which is remarkable and one of the reasons that in 1D MPS is successful. How this effects the TTN approach will be explained in section 3.1

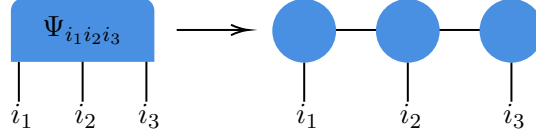


Figure 2.9: Decompose $|\Psi_{i_1 i_2 i_3}\rangle$ to an MPS

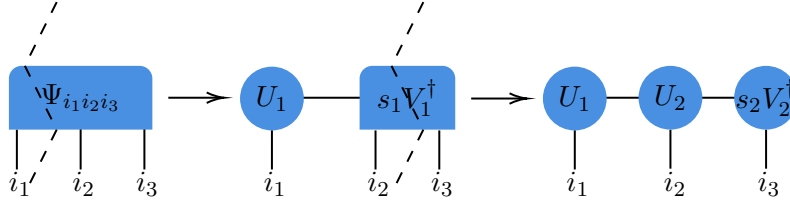


Figure 2.10: Decomposition of $|\Psi_{i_1 i_2 i_3}\rangle$ into its left-canonical MPS form. Dashed line represents application of a SVD

2.4.4 Canonicity

In order to compute expectation values efficiently or equivalently apply operators to the MPS ansatz one needs to put the MPS in a so called *canonical-form*. A MPS can either be put in *left*, *right*, or *mixed* canonical form. Let us say we have a simple state $|\Psi_{i_1 i_2 i_3}\rangle$ which we wish to decompose into a MPS consisting of three tensors as depicted in figure 2.9. In order to put the MPS in a one of these canonical forms one can either start by applying SVD's or QR-decomposition's (QRD's) on the MPS of which the former is depicted in figure 2.10 where a left-canonical MPS is created. The decomposition of $|\Psi_{i_1 i_2 i_3}\rangle$ into its right-canonical form is similar but then the SVD's are applied starting from the right. Aside from the left - and right-canonical forms one can also create a mixed-canonical form, which as the name suggests has both forms with respect to some tensor M , an example using the MPS in 2.10 is given in figure 2.11. Important to note is that one can insert any invertible matrix A as $A^{-1}A$ into the link between two tensors M and N , since $A^{-1}A = \mathbb{1}$, which can be thought of as a *gauge*-freedom of the MPS, which in turn can also be incorporated in the TTN ansatz as will be explained in slightly different context in section 3.2.2. When computing the norms ($\langle \Psi_{i_1 i_2 i_3} | \Psi_{i_1 i_2 i_3} \rangle$) of for example the decomposition in figure 2.11 multiple tensors do not need to be contracted due to their unitarities, which is illustrated in figure 2.12. This is useful for the computation of expectation values of (local) operators as will be explained in the next section.

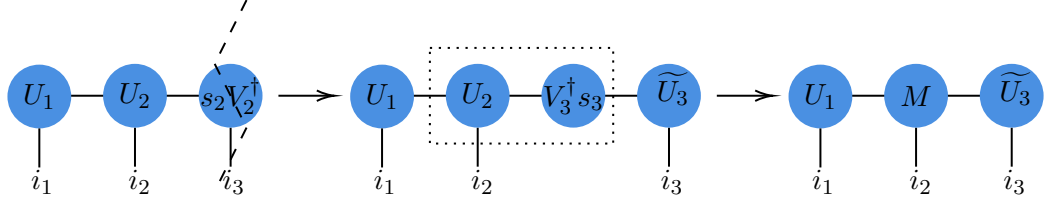


Figure 2.11: Changing the left-canonical MPS in 2.10 to its mixed-canonical form

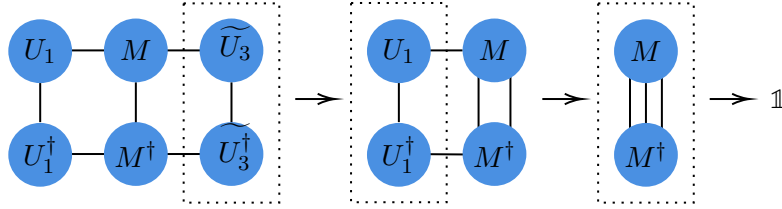


Figure 2.12: Norm of mixed-canonical MPS of $|\Psi_{i_1 i_2 i_3}\rangle$

2.4.5 Computation of expectation values

Since it is clear how one can obtain a MPS from a state we can develop an approach on how to compute expectation values in the MPS ansatz. Consider for instance the expectation value of some local operator o_s acting on i_2 of $|\Psi_{i_1 i_2 i_3}\rangle$, which has been put in mixed-canonical form. Due to the canonicity of the MPS the amount of tensors needed to compute the expectation value of o_{i_2} is reduced to just 3 as depicted in figure 2.13.

2.4.6 Simple optimisation

Tensor Network ansatzes are variational ansatzes, meaning that the approximated ground-state energy found after the optimisation is an upper bound

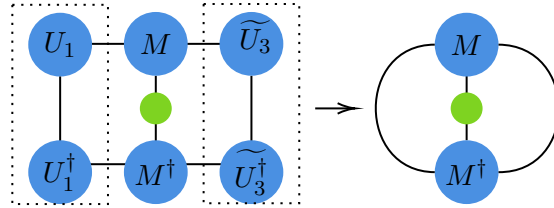


Figure 2.13: $\langle \Psi_{i_1 i_2 i_3} | o_{i_2} | \Psi_{i_1 i_2 i_3} \rangle$

to the true ground-state energy. In this section an example on how to optimise a small MPS and is explained and is meant to be instructive. A more elaborate explanation in the context of the Tree Tensor Network is given in section 4.2. Now that the basic concepts of the simple tensor network ansatz, the MPS, should be understood, it is straightforward to explain how to optimize a network in order to do e.g. groundstate calculations. Let us assume that the tensor network to be optimized is of the form as the one in 2.11. Then the optimisation is done as follows:

1. Depending on the type of update (single- or two-site update) start at a site(s) $i(j) = 1$ and minimize the energy with respect to the site(s), meaning that tensors at other sites are *fixed*.
2. Repeat step 1 for every site.
3. Repeat step 1,2 until the energy $\langle \Psi | H | \Psi \rangle$ has converged

Minimising the energy with respect to some tensor M is done by taking the derivative with respect to M and equating it to 0 after having added a lagrange multiplier to ensure that the norm of Ψ is preserved:

$$\frac{\partial}{\partial M} (\langle \Psi | H | \Psi \rangle - \lambda \langle \Psi | \Psi \rangle) \quad (2.12)$$

Taking the derivative with respect to M is equivalent to leaving U_1 out of equation 2.12, which leads to a tensor network illustrated in figure 2.14. The problem can then be reduced to a simplified eigenvalue problem if and only if the network is put in mixed-canonical form with respect to U_1 , else the problem will be a generalized eigenvalue problem.

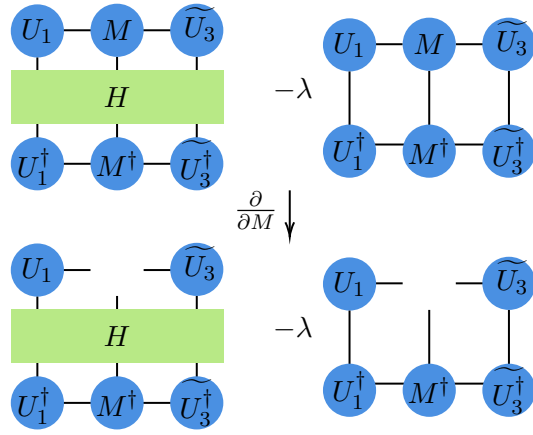


Figure 2.14: Tensor network corresponding to applying equation 2.12 to the network in 2.11

Chapter 3

Tree Tensor Network Ansatz

3.1 Introduction

The goal of the TTN ansatz is to effectively describe a pure state $|\Psi\rangle \in V^{\otimes N}$ of some lattice \mathcal{L} by means of a tensor network in a tree form.

A very intuitive interpretation of the Tensor Network ansatz is the coarse graining transformation of some lattice into a coarser grained lattice. Starting with some lattice \mathcal{L} , the TTN defines a series of coarser grained lattices $\{\mathcal{L}_0, \mathcal{L}_1, \dots, \mathcal{L}_{T-1}\}$. Each site in \mathcal{L}_T is defined in terms of sites \mathcal{L}_{T-1} by the mapping of an *isometry* w_T , which will be explained in section 3.2. For a graphical interpretation of the coarse graining transformation and the corresponding diagrammatic version of the network see figure 3.1. Although this coarse graining transformation is related to the *real space Renormalization Group* initially proposed by Kadanoff, Migdal and Wilson [24], [26], [58], [15], [5], and [25], the approach with the TTN is different. In real space RG the idea is to follow some *spin blocking* scheme that results in finding an effective Hamiltonian to a block of sites, H_B and then choosing the isometries such that the local subspace corresponding to the lowest eigenvalues of H_B is preserved. In the TTN ansatz, however, the isometries are chosen using a seed for the random-number generator, which forces us to globally minimise H . This closely resembles the initial proposal of White's DMRG. Elaborating on the definition of the entanglement entropy in equation 2.10, the entropy of a generic state of block A of \mathcal{L} , is proportional to the number of sites $n(A)$.

$$S(A) = n(A) \log d \quad (3.1)$$

Which for some lattice consisting of $l \times l$ sites is quadratic in l for which the effective site dimension, read: bond dimension, χ is exponential in l^2 , namely

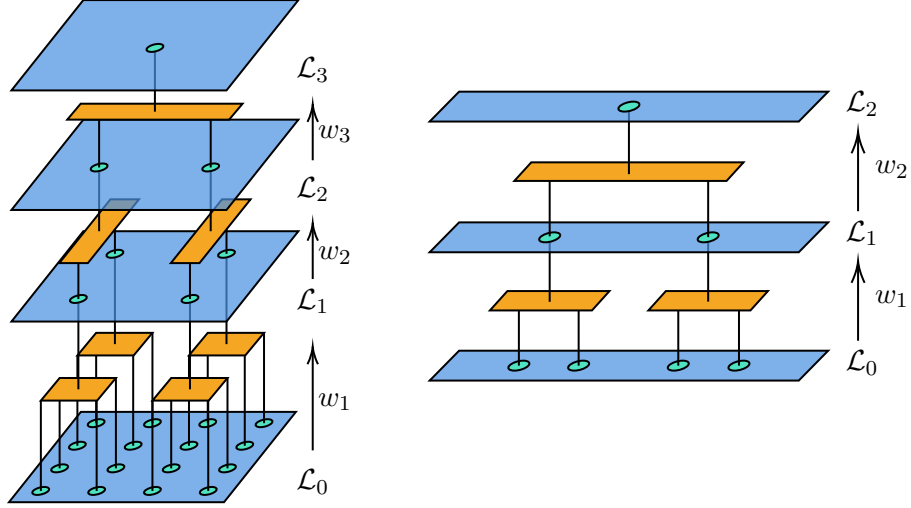


Figure 3.1: (a): coarse graining transformation of a square lattice \mathcal{L}_0 starting from 16 sites to effectively 1 site in \mathcal{L}_3 which is used to encode a subspace $\mathcal{V}^{\otimes N}$ in the TTN instead of $|\Psi\rangle$. The coarse graining transformation is realized as follows: every 4 sites in \mathcal{L}_0 correspond to 1 site in \mathcal{L}_1 , every 2 sites in \mathcal{L}_1 correspond to 1 site in \mathcal{L}_2 and all sites in \mathcal{L}_2 correspond to the last site in \mathcal{L}_3 , which therefore contains all information of the entire lattice. (b): coarse graining transformation of a $1D$ chain

$\chi \sim d^{l^2}$. However, as already mentioned in section 2.4.3, the entanglement entropy of groundstates of local Hamiltonians typically scale with its area, $S(A) \sim c\Sigma(A)$, $\Sigma(A)$ being the interacting boundary of block A . Assuming toroidal boundary conditions, the entropy scales as $S(A) \sim 4cl$, giving a lower bound on the bond-dimension: $\chi_{l \times l} \geq \exp(4cl)$. The latter being the a justification that one can approximate a ground-state $|\Psi\rangle$ that fullfills the area law, due to χ scaling as $\mathcal{O}(\exp(L))$ instead of $\mathcal{O}(\exp(L^2))$, despite the fact the TTN ansatz does not reproduce an area law.

3.2 Tree Tensor Network Ansatz

3.2.1 Isometries

The tensors that build the TTN have at least 2 physical legs and at most 1 bond leg as shown in figure 3.2, and are constraint to being isometric in the

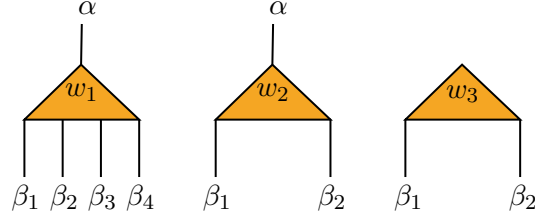


Figure 3.2: Tensors in TTN of figure 3.1

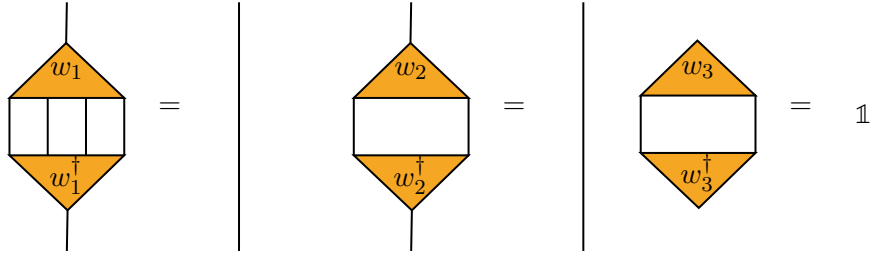


Figure 3.3: Isometric constraints for tensors in 3.1

following sense.

$$\sum_{\beta_1 \dots \beta_n} (w)_{\beta_1 \dots \beta_n}^\alpha (w^\dagger)_{\alpha'}^{\beta_1 \dots \beta_n} = \delta_{\alpha \alpha'} \quad (3.2)$$

Applied to the example of the coarse graining transformation in figure 3.2 gives the following constraints

$$\begin{aligned} \sum_{\beta_1 \beta_2 \beta_3 \beta_4} (w_1)_{\beta_1 \beta_2 \beta_3 \beta_4}^\alpha (w_1^\dagger)_{\alpha'}^{\beta_1 \beta_2 \beta_3 \beta_4} &= \delta_{\alpha \alpha'} \\ \sum_{\beta_1 \beta_2} (w_2)_{\beta_1 \beta_2}^\alpha (w_2^\dagger)_{\alpha'}^{\beta_1 \beta_2} &= \delta_{\alpha \alpha'} \\ \sum_{\beta_1 \beta_2} (w_3)_{\beta_1 \beta_2}^\alpha (w_3^\dagger)_{\alpha'}^{\beta_1 \beta_2} &= 1 \end{aligned}$$

which in diagrammatic notation yield the constraints shown in figure 3.3. Tensors that obey these constraints are referred to as *isometries*. The use of isometries reduces the complexity of the TTN significantly as will be further explained in the section on the computation of operators (3.3) and their properties can be seen as if they prevent numeric instabilities during the optimisation process. For now let us first illustrate the TTN corresponding to the example of figure 3.1.

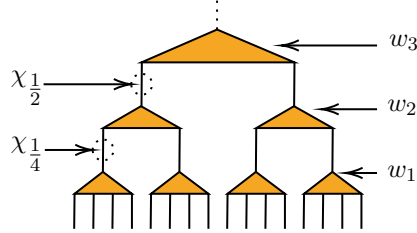


Figure 3.4: TTN decomposition of $|\Psi_{i_1 \dots i_{16}}\rangle \in \mathbb{V}^{d^{16}}$

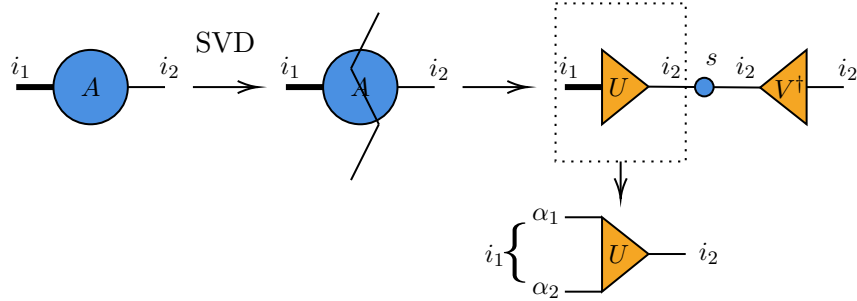


Figure 3.5: Initialization of an isometry, starting with a random matrix A one can perform an SVD to obtain a matrix U , which fullfills the isometric constraints in equation 3.2 after reshaping U into a rank 3 tensor

The $\chi_{\frac{1}{2}}$ and $\chi_{\frac{1}{4}}$ denote the bond dimension which connect the isometries from one layer to another. For the initialization of isometries one can create some random non-square matrix A , apply a SVD on $A = UsV^\dagger$, and take U by reshaping it back into a rank 3 tensor, see figure 3.5

3.2.2 Canonical form

Although in this thesis only the TTN decomposition into isometries is used, it is worth mentioning that one can in principle use other realisations by means of an exact decomposition, read: full Schmidt decomposition, or by using a TTN form where the decomposition is *canonical*. This means that one inserts *link matrices* σ (identities) between legs of tensors, internal indices, folowed by an orthogonalization by adding unitary matrices between

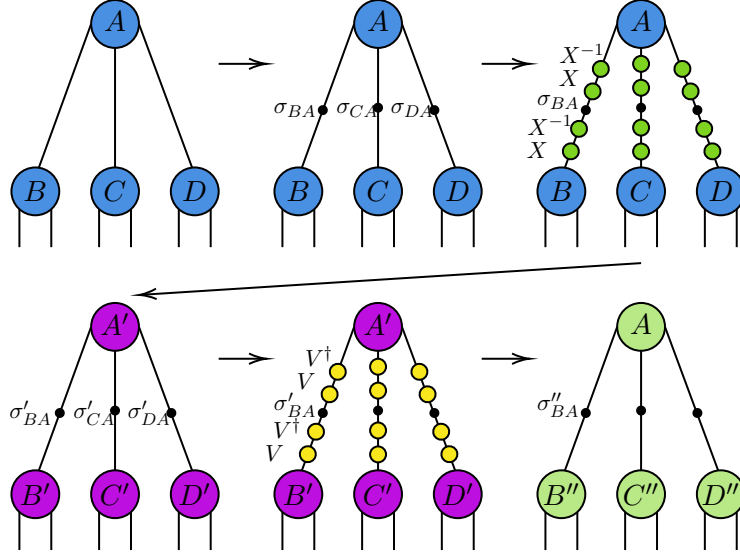


Figure 3.6: Process of putting a tree tensor network in canonical form

σ and the tensors σ is connected to: $AXX^{-1}\sigma XX^{-1}B$ where X is obtained by calculating the reduced density matrix ρ of the branch of the tree σ is in and taking the *principal* square root, equivalently the decomposition of ρ into XX^{-1} . Then one absorbs the X and X^{-1} into the tensors according to $AXX^{-1}\sigma XX^{-1}B = A'\sigma'B'$ followed by an SVD on σ' where the matrices U and V^\dagger are absorbed into A and B , $A'UU^\dagger\sigma VV^\dagger B' = A''\sigma''B''$. For an example, see figure 3.6. Eventually, when having done this to every tensor in the network, the entire network is in canonical form. Although this takes some extra steps to perform before being able to optimise the network and/or extract relevant data out of it (expectation values etc), one of the benefits is that *every* tensor is isometric with respect to the tensor one wants to extract information out of.

3.3 Computation of Operators

3.3.1 one- and two-site operators

The computation of operators is very straightforward in the isometric TTN ansatz. Let us first notice that in the ansatz and given a TTN decomposition of $|\Psi\rangle$ in isometries the norm is always preserved, or equivalently:

$$\langle\Psi|\Psi\rangle = 1$$

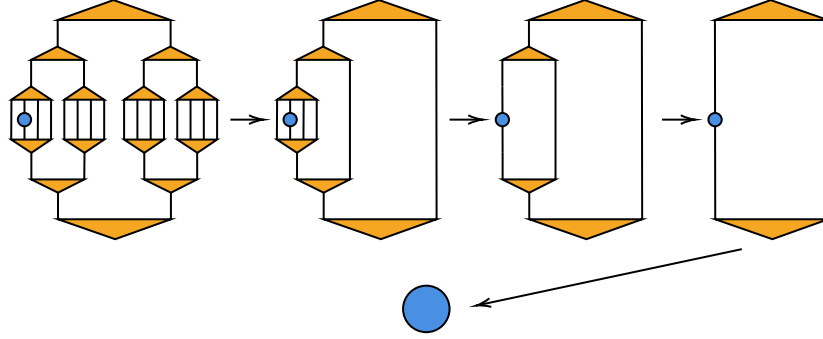


Figure 3.7: Computation of an expectation value $\langle \Psi | o^s | \Psi \rangle$

Which means that the TTN does not need to be in a canonical form unlike forms of TTNs where the tensors are not isometric. Furthermore given an operator O^s that acts locally on the a site s , the expectation value is given by:

$$\langle \Psi | O^s | \Psi \rangle \quad (3.3)$$

Which can be computed by contracting the corresponding network as illustrated in figure 3.7. Due to the isometries most of the contractions do not have to be performed since the isometric constraints ensures that these contractions result in identities. Similarly for two-site operators one can decompose the product into a sum of one site operators as

$$O^{ss'} = \sum_{ss'} o^s o^{s'} \quad (3.4)$$

if the initial two-site operator acts on two different sites of $|\Psi\rangle$. In general one can always decompose any product of one-site operators $\langle \Psi_{1\dots n} | o^1 \dots o^n | \Psi_{1\dots n} \rangle$ into a sum of one-site operators. See figure 3.8 for how the contraction concerning the computation of a two-site operator, $\langle \Psi | o^s o^{s'} | \Psi \rangle$, is performed.

3.3.2 Reduced density matrix

Apart from one-site and two-site operator expectation values, reduced density matrices are also very straightforward to obtain in the TTN ansatz. For the example of the 4×4 lattice one can immediately given the decomposition of a state $|\Psi\rangle$ obtain the $\rho_{sub-lattice}$ by tracing out the environment of the sub-lattice. Consequently one can easily obtain the spectral decomposition of ρ as depicted in figure 3.9.

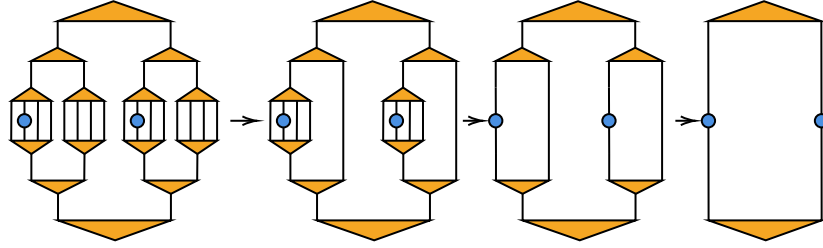


Figure 3.8: Computation of an expectation value $\langle \Psi | o^s o^{s'} | \Psi \rangle$

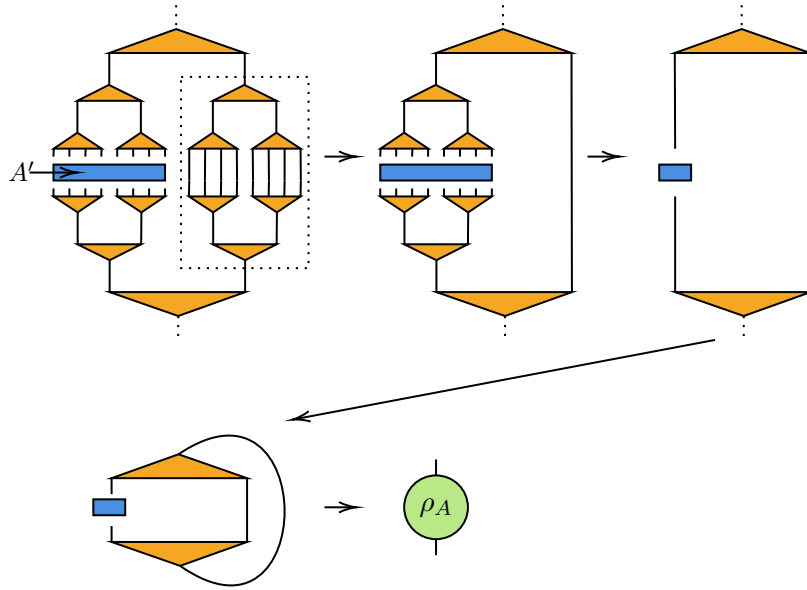


Figure 3.9: Computation of the reduced density matrix of block A of lattice \mathcal{L}_{AB}

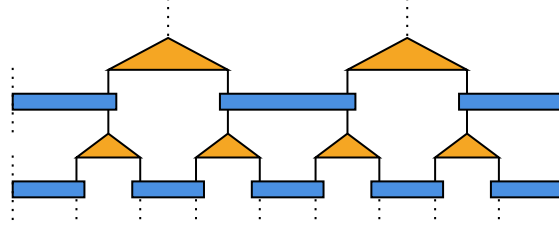


Figure 3.10: 2 layers of a typical binary-MERA. The blue rectangles represent the disentanglers and the yellow triangles the isometries (coarse-grainers).

3.3.3 Relation to MERA

The TTN has a similar structure as the MERA (Multiscale Entanglement Renormalization Ansatz) [10, 12], an ansatz designed to reproduce the $\log(L)$ scaling for the entanglement entropy of 1D critical states which the TTN ansatz is not able to reproduce. To achieve this disentanglers are introduced, tensors that are ought to remove short range entanglement which are defined as:

$$u : \mathcal{V}^{\otimes N} \rightarrow \mathcal{V}^{\otimes N} \quad (3.5)$$

With the property:

$$u^\dagger u = uu^\dagger = \mathbb{1} \quad (3.6)$$

The TTN ansatz for 1D systems can be thought of as a MERA, depicted in figure 3.10, where the disentanglers have been replaced by identities. Since the dominant scaling in the TTN is of order $\mathcal{O}(\chi^4)$, and the scaling of the MERA is of order $\mathcal{O}(\chi^{16})$, for small values of χ the TTN has a better scaling than the MERA, yet for increasing size of 2D systems the benefit of using the TTN is negated by the need of a large bond dimension to obtain accurate results.

3.3.4 Implementing symmetries

The implementation of translational symmetries in the TTN ansatz is straightforward. One can for instance implement a translational symmetry by choosing the isometries of a given coarse-grained lattices to be the same. This leads to a significant reduction in computational time since only 1 tensor in each layer has to be optimised. However, the implementation of other symmetries such as $U(1)$, \mathbb{Z}_2 , and \mathbb{Z}_3 require more preparation of the tensors and are not that straightforward [42].

Chapter 4

Methods

4.1 Introduction

In this chapter the optimisation strategy for the TTN is explained by means of a simple example Hamiltonian consisting of two-site operators $o^{ss'}$ which are decomposed into a sum of a product of one-site operators. The isometric gauge is used and exploited in the optimisation strategy. Then the application to the models studied in this thesis are introduced and explained following a notion of some caveats during the optimisation process.

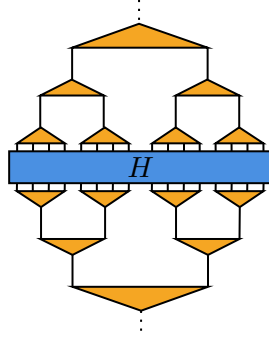


Figure 4.1: $\langle \Psi_{w_i} | H | \Psi_{w_i} \rangle$ for $i \in \{1, 2, 3\}$

4.2 Optimisation strategy

4.2.1 Cost-function

First let us introduce the function which is optimised and illustrate in short the complexity of finding a solution. Having initialised a TTN with fixed bond dimensions χ the cost function to be minimised is given by the expectation value of the Hamiltonian:

$$E(\{w_i\}) \equiv \langle \Psi_{w_i} | H | \Psi_{w_i} \rangle \quad (4.1)$$

Which is depicted as the contraction in figure 4.1 and $\{w_i\}$ is the set of isometries of the TTN to be optimised such that one approximates the optimal ground-state energy of H , $E(\{\bar{w}_i\})$ and the corresponding optimal TTN state $|\Psi_{\bar{w}_i}\rangle$ to the groundstate $|\Psi_{GS}\rangle$ by finding the minimum of equation 4.1:

$$E(\{\bar{w}_i\}) \equiv \min_{\{w_i\}} \langle \Psi_{w_i} | H | \Psi_{w_i} \rangle \quad (4.2)$$

Due to the non-linearity of the above equation, an *exact* solution to this equation is not known. However, one can try to approximate the ground-state energy by means of an *iterative* optimisation strategy that minimizes equation 4.1 as introduced in [11] and [47].

Given the set of isometries $\{w_1, w_2, \dots, w_n\}$ that build the TTN state and are initialised *randomly*, one first optimises one of the isometries, say w_1 , whilst keeping all others *fixed*, resulting in a new $w_1 \rightarrow w'_1$, then one proceeds using the updated set $\{w'_1, w_2, \dots, w_n\}$ to find the next w'_i until all isometries in the set are updated. This defines one sweep, which is repeated until the cost function seems to have converged by setting a *convergence criterion*. The latter can differ for different system sizes. In order to check the convergence of the energy during the optimisation one can impose different criteria depending on the model used and the dimensionality of the system. For small lattices (2D) and chains (1D) a simple energy difference criterion can be used, although this is not recommended and not very useful. Instead imposing a minimum variance criterion by sampling over the last N computed energies giving $\{E_{N-3}, E_{N-2}, E_{N-1}, E_N\} = \mathcal{E}$ and demanding $Var(\mathcal{E}) < \epsilon$ is more effective since the energy difference can have a minimum that is larger than zero. Furthermore, in this thesis the variance criterion is applied to *every* system of any size, since in practice it can lead to a significant reduction in iterations if the energy is already close to its value. It is worth mentioning that the minimum of equation 4.1 is an upper limit to its global minimum, implying that if one finds a smaller energy - a lower minimum - that the resulting minimum is a better solution.

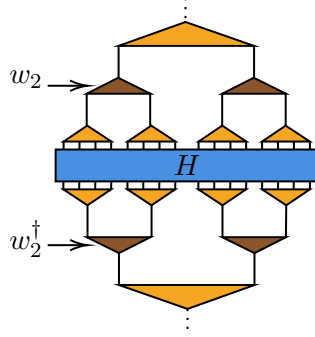


Figure 4.2: Optimisation of isometries in second layer, starting with w_2

4.2.2 Optimisation of an isometry

In this section the optimisation of a single isometry in the TTN is explained. Let us first recall that as already mentioned in section 3.3.1 if one has an Hamiltonian consisting of two-site terms one can always express that in terms of one-site operators. So given the cost function:

$$E(\{w_i\}) = \sum_{\langle s, s' \rangle} E^{ss'}(\{w_i\}) \equiv \sum_{\langle s, s' \rangle} \langle \Psi_{\{w_i\}} | h^{[s, s']} | \Psi_{\{w_i\}} \rangle \quad (4.3)$$

Then if one wants to optimise say isometry w_2 of the example in figure 4.1 as depicted in figure 4.2, one views the cost function as a function depending on one isometry w namely:

$$E(w) = F(w) + G \quad (4.4)$$

Where F collects all the contributions of H within its sub-lattice (read: block A) and G collects all two-site terms outside of that sub-lattice and hence is a constant. As illustrated in figures 4.3, 4.4, and 4.5, the two-site terms decomposed into one-site terms acting on s and s' can either be both in A , one in A , or neither in A . In the latter case when both are in $E^{[s, s']}$ yet are not in block A then due to the isometric constraint of w , the contraction of w with w^\dagger cancels out. This results in G in equation 4.4 being a constant and therefore it can be ignored during the optimisation of w . In the former case, however, when either one of s , s' or both are in block A one can decompose $F(w)$ into two parts:

$$F(w) = F_{AA}(w) + F_{AB}(w) \quad (4.5)$$

Where $F_{AA}(w)$ collects terms where both occur in block A , and $F_{AB}(w)$ collects terms where one term is in block A whilst the other is in block B . Then the optimisation translates to finding the minimum of F :

$$\min_w F(w) \quad (4.6)$$

Which, again, has no exact solution known. therefore one must linearize $F(w)$ in w by considering the latter to be independent of its hermitian conjugate, w^\dagger . This leads to a simple cost function $I(w)$ which we minimize with respect to w :

$$\min_w F(w) \approx \min_w I(w) = \min_w \text{Tr}(\Gamma w) \quad (4.7)$$

$\Gamma = UsV^\dagger$ being the SVD of the environment of w . For $I(w)$ an exact solution that minimizes it, is known. The latter being $w = -VU^\dagger$ which results in:

$$\begin{aligned} \min_w I(w) &= \min_w \text{Tr}(\Gamma w) = \min_w \text{Tr}(-UsV^\dagger VU^\dagger) \\ &= \min_w \text{Tr}(-sV^\dagger VU^\dagger U) \\ &= \min_w \text{Tr}(-s) = -\sum s \end{aligned}$$

Which obviously minimizes $I(w)$. Now all that is left is to explain how one obtains the environment, Γ , of w . Similar to how it is done for $F(w)$, one splits the environment of w into two parts:

$$\Gamma(w) = \Gamma(w)_{AA} + \Gamma(w)_{AB} \quad (4.8)$$

Where just like in $F(w)$, $\Gamma(w)_{AA}$ collects contributions where both one-site-terms occur in A and likewise $\Gamma(w)_{AB}$ collects contributions where either one one-site-term occurs in A and the other occurs in B . Two examples for both $\Gamma(w)_{AA}$ and $\Gamma(w)_{AB}$ are given in figures 4.6 and 4.7 respectively. With the optimal solution for w' , w^\dagger is replaced by w'^\dagger in $F(w)$ which leads to an updated environment Γ' . This process is iterated and results in a set of isometries $\{w', w'', w''', \dots\}$ which in general leads to a decreasing $F(w)$, that is $F(w') \geq F(w'') \geq \dots$

4.2.3 Cost of optimisation

The cost of optimizing an isometry is determined by the costs of computing its environment, the model used, and the SVD on its environment which

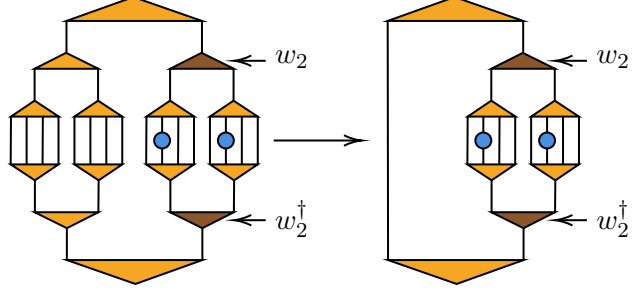


Figure 4.3: Contraction where both one-site terms coming from $h^{[s,s']}$ are in $F_{AA}(w_2)$

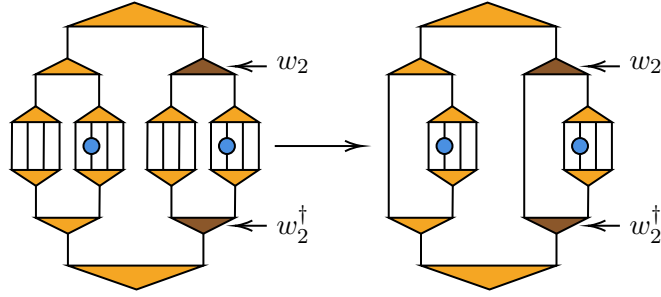


Figure 4.4: Contraction where one one-site terms coming from $h^{[s,s']}$ is in $F_{AA}(w_2)$ and the other is in $F_{AB}(w_2)$

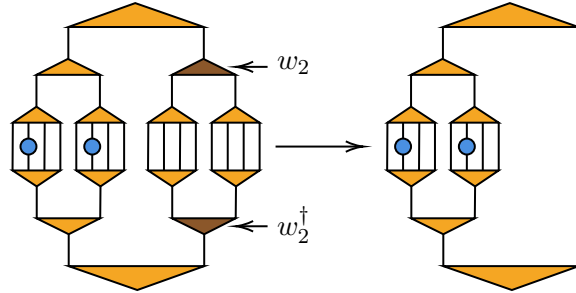


Figure 4.5: Contraction where both terms coming from $h^{[s,s']}$ appear in block B and thus contribute to the constant G

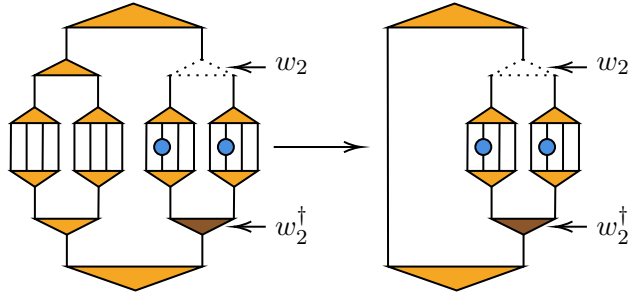


Figure 4.6: Environment term contributing to $\Gamma(w)_{AA}$ in equation 4.8

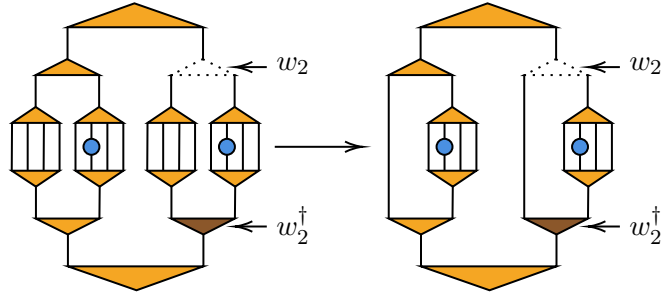


Figure 4.7: Environment term contributing to $\Gamma(w)_{AB}$ in equation 4.8

in turn depends on the layer the isometry is in. Assuming that the bond-dimensions are the same for all layers except the bottom layer, the cost of optimizing the entire TTN scales as $\mathcal{O}(L\chi^4)$ where L is the contribution of two-site terms on the boundary between two halves of the system. The cost of the SVD on the environment of an isometry scales as χ^4 . The overall costs can be reduced by the implementation of translational symmetry albeit with a reduced multiplicative pre-factor. If the model, however, consists of long-range interactions such as a model where every site interacts with every other site the order of L in the costs increases to 4 leading to an overall cost that scales as $\mathcal{O}(L^4\chi^4)$ since there are L^4 terms contributing to the Hamiltonian.

Chapter 5

Models

5.1 Introduction

In this chapter the Transverse Field Ising model (TFI), for both 1D and 2D, and the J_1 - J_2 Heisenberg model are explained. The TFI model serves as an excellent benchmark model due to its simplicity yet richness to physics whilst the J_1 - J_2 Heisenberg model is heavily studied since its phase-diagram, more specifically the point at maximal frustration $J_1 = 2J_2$, is not fully understood yet. The chapter is build up as follows, first the TFI is presented along with an explanation of its phase diagram. Then the J_1 - J_2 Heisenberg model is explained along with its phase-diagram by first looking at its classical version and then expanding to its quantum form by reintroducing the off-diagonal terms.

5.2 Transverse field Ising model

Hamiltonian

The transverse field Ising model is given by the following Hamiltonian:

$$H = -J \sum_{\langle i,j \rangle} \sigma_x^i \sigma_x^j - \lambda \sum_i \sigma_z^i \quad (5.1)$$

Where $\sigma_n, n \in (x, y, z) = \left\{ \begin{pmatrix} 0 & 1 \\ 1 & 0 \end{pmatrix}, \begin{pmatrix} 0 & -i \\ i & 0 \end{pmatrix}, \begin{pmatrix} 1 & 0 \\ 0 & -1 \end{pmatrix} \right\}$ are the pauli matrices, λ is the magnetic field strength, J is the two-site coupling strength, and $\langle i, j \rangle$ denotes the nearest neighbour interactions on i, j .

Phase-diagram

The parameters λ and J are used to tune the system and study the behaviour at different values. For $J < 0$ the system is said to be *anti-ferromagnetic* whereas for $J > 0$ the system is *ferromagnetic*. Due to its simplicity the transverse-field Ising model is often used to benchmark results, as it will be for the TTN ansatz in this thesis.

In 1D the model is known for undergoing a phase transition at the *QCP* $\lambda = 1$ and an exact solution is known [44]. For 2D systems Monte Carlo (MC) simulations, using an application of a continuous time cluster algorithm, have shown that the system undergoes a phase transition around $\lambda = 3.044 \approx 3$ [40]. Systems at critical points are highly entangled and therefore should have the highest entanglement entropy around these points. For both 1D and 2D the model is in an ordered phase below λ_c and becomes disordered for $\lambda > \lambda_c$. Since, in this work, finite lattices are used it is worth mentioning that the λ_c 's are shifted and they reach λ_c only in thermodynamic limit where $L \rightarrow \infty$. Furthermore for finite lattices we expect the magnetization in the x -direction, $m_x = \frac{1}{N} \sum_i \sigma_x^i$, to be zero since for every configuration leading to a magnetization of $-M$ there exists a configuration where the magnetization is $+M$. Only in the thermodynamic limit where this symmetry is spontaneously broken the magnetization is found to be non-zero.

A way to identify these phases is by studying the spin-spin correlators on the lattice, more specifically the maximum distance correlators which are, for the 1D TFI, defined as:

$$C(i, L/2) = \langle \sigma_x^i \sigma_x^{i+L/2} \rangle - \langle \sigma_x^i \rangle \langle \sigma_x^{i+L/2} \rangle \quad (5.2)$$

and for the 2D TFI defined as:

$$C(i, j + L/2) = \langle \sigma_x^{i,j} \sigma_x^{i,j+L/2} \rangle - \langle \sigma_x^{i,j} \rangle \langle \sigma_x^{i,j+L/2} \rangle \quad (5.3)$$

$$C(i + L/2, j) = \langle \sigma_x^{i,j} \sigma_x^{i+L/2,j} \rangle - \langle \sigma_x^{i,j} \rangle \langle \sigma_x^{i+L/2,j} \rangle \quad (5.4)$$

Since at λ_c in the thermodynamic limit we expect the long range correlators to remain large, which for finite systems translates into non zero maximum distance correlators, and these correlators are expected to decay as λ increases. More specifically, the correlators are expected to decay exponentially $\propto \exp\{-r/\xi\}$ as a function of the distance and the correlation length ξ away from λ_c and decay $\propto r^{-(d-2+\eta)}$ at λ_c . For finite systems, if we are far away from λ_c the correlation length ξ is finite and the finite size

effects can be neglected. As λ approaches λ_c the correlation length should diverge in the thermodynamic limit, however since the systems sizes are finite and the correlation length is therefore bounded by L , this can not occur. This results in the absence of a sharp phase transition and in a smeared out transition around λ_c .

5.3 Heisenberg J_1 – J_2 model

5.3.1 Introduction

Frustrated magnetism has become significantly more active in the recent decades due to Anderson's *Resonating Valence Bond theory* [1] which aims to explain the physics of high-temperature superconductors, which are of great interest due to their characterizing property to have vanishing electrical resistance below some critical temperature T_c . Current day studies [51, 57] heavily focus on nature of the phase diagrams of spin lattice models that could give rise to such properties via a so called *Quantum Spin Liquid* phase (QSL), which has the interesting property to have excitations in form *fractons*, more specifically *spinons*, that are quasi-particle excitations. In addition these QSLs also have vanishing long range conventional order.

One of the models that could give rise to a QSL is the $J_1 - J_2$ Heisenberg model on a square lattice as it experiences maximal frustration around the ratio $J_1 = 2J_2$. However, in order to understand what constitutes to a QSL some concepts such *Valence Bond States* and *Valence Bond Crystals* should be explained. Furthermore it is useful to first discuss the *classical* $J_1 - J_2$ model, by working only in the z-basis and omitting the off-diagonal terms, and its ground-states and then discuss what happens as they enter the Hamiltonian again and induce quantum fluctuations.

Hamiltonian

The J_1 - J_2 Heisenberg model is given by the following Hamiltonian:

$$H = J_1 \sum_{\langle i,j \rangle} \vec{S}_i \cdot \vec{S}_j + J_2 \sum_{\langle\langle i,j \rangle\rangle} \vec{S}_i \cdot \vec{S}_j \quad (5.5)$$

Where, again, $\langle i, j \rangle$ denotes the nearest-neighbour (NN) interaction which is controlled by the coupling strenght J_1 and in addition there is a *next-nearest-neighbour* (NNN) term denoted by $\langle\langle i, j \rangle\rangle$ and controlled by the paramter J_2 , see figure 5.1. \vec{S}_i are the spin-operators, which for spin $\frac{1}{2}$ particles reduce to the pauli-matrices according to:

$$\begin{aligned} S_x &= \frac{1}{2}\sigma_x, \\ S_y &= \frac{1}{2}\sigma_y, \\ S_z &= \frac{1}{2}\sigma_z \end{aligned}$$

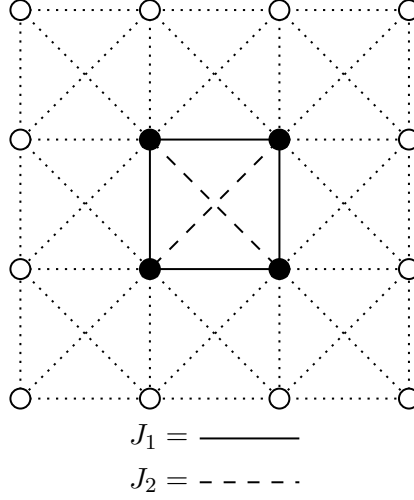


Figure 5.1: Illustration of the lattice form of the $J_1 - J_2$ Heisenberg model

Where \hbar is set to 1 on the RHS of the equations above. Another form is where one works in the z-basis and the spin-operators have been expressed in terms of *ladder-operators* S_+ and S_- which are defined by:

$$S_x = \frac{1}{2} (S_+ + S_-) \quad (5.6)$$

$$S_y = \frac{1}{2i} (S_+ - S_-) \quad (5.7)$$

$$(5.8)$$

and in the spin $\frac{1}{2}$ the matrix forms are:

$$S_+ = \begin{pmatrix} 0 & 1 \\ 0 & 0 \end{pmatrix} \quad (5.9)$$

$$S_- = \begin{pmatrix} 0 & 0 \\ 1 & 0 \end{pmatrix} \quad (5.10)$$

Allowing us to rewrite the Hamiltonian in 5.5 to:

$$\begin{aligned}
 H = & J_1 \sum_{\langle i,j \rangle} \left[\frac{1}{2} (S_i^+ S_j^- + S_i^- S_j^+) + S_i^z S_j^z \right] \\
 & + J_2 \sum_{\langle i,j \rangle} \left[\frac{1}{2} (S_i^+ S_j^- + S_i^- S_j^+) + S_i^z S_j^z \right]
 \end{aligned}$$

Phase-diagram

In order to get a clear picture on what constitutes to the phase-diagram of the model described in the previous section, let us first look into what its classical version has to offer by ignoring all off-diagonal terms that contribute to the Hamiltonian, meaning we restrict ourselves to the following classical Hamiltonian in the z-basis:

$$H = J_1 \sum_{\langle i,j \rangle} S_i^z S_j^z + J_2 \sum_{\langle\langle i,j \rangle\rangle} S_i^z S_j^z \quad (5.11)$$

Let us first consider the limit $J_1 \gg J_2$ where the NN couplings dominate over the NNN couplings. Then the ground-state has an AF order characterised by a checker-board pattern consisting of alternating spin sign, referred to as the *Néel AF* phase. As soon as we turn J_2 on, the lattice becomes frustrated due to NN and NNN bonds not being fully saturated. In order to quantify the physics as we adjust J_2 let us define the *spin-spin* correlators:

$$C_s(x, y) = \langle \mathbf{S}_{0,0} \cdot \mathbf{S}_{x,y} \rangle = \frac{1}{N} \sum_{i,j} \mathbf{S}_{i,j} \mathbf{S}_{i+x,j+y} \quad (5.12)$$

Where the values $x = y = L/2$ are of most interest since the corresponding correlator signifies the long-range order of the system and due to the finite sizes of the systems we wish to take L as large as possible. Another form which is used more often is equation 5.12 its Fourier transformed form, also referred to as a *structure factor*:

$$S_s(\mathbf{q}) = \frac{1}{N^2} \sum_{i,j} \exp\{i\mathbf{q}(\mathbf{r}_i - \mathbf{r}_j)\} C_s(i, j) \quad (5.13)$$

Where $\mathbf{r}_i = (x_i, y_i)$ and \mathbf{q} is the wave vector. Structure factors enable us to identify spin structures on the lattice of a finite size, which are also ought to occur on lattices of larger sizes.

So what happens when in the other limit where $J_1 \ll J_2$? Let us start with $J_1 = 0, J_2 \neq 0$, then the sublattices that define the total lattice become decoupled in the sense that they independently exhibit Néel orderings. Now let us consider a finite value for J_1 , yet still $J_1 \ll J_2$. The NN couplings will be saturated since such configurations lead to a lower total energy, resulting in a *Stripe AF* order which classically, without the off-diagonal terms, consists of two orderings: vertical and horizontal stripe orders. Now let us consider the maximally frustrated point in the phase diagram

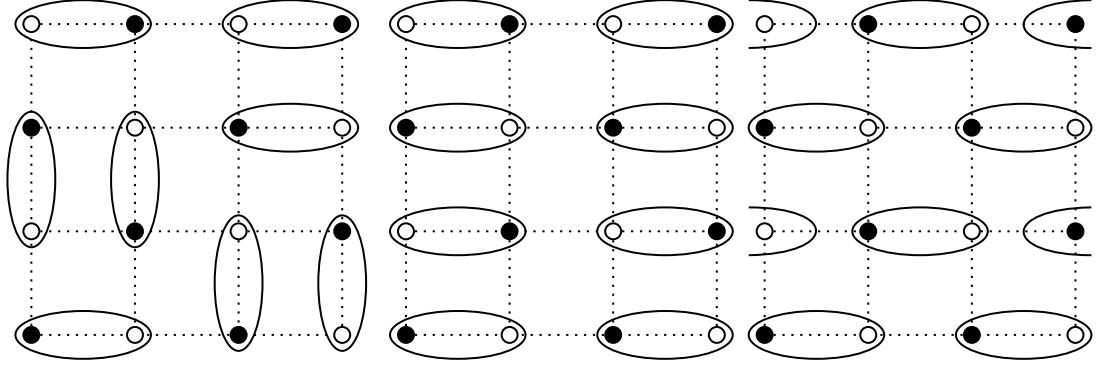


Figure 5.2: Examples of dimer-singlets on a 4×4 lattice. The black and white points depict the spin-up and spin-down orientations. From left to right: Random dimer order, VBC, and a staggered VBC

$J_1 = 2J_2$. To see why it is exactly this point where the system maximally frustrated consider configurations in both the Néel and the Stripe AF phase. $J_1 = 2J_2$ implies one can exchange a single NN couple with two NNN couples, similarly if one for instance takes all four NN bonds for a given site one can exchange these for two NN bonds and four NNN bonds without changing the energy of the configuration. More specifically, one can tile these NN bonds and the NNN bonds to create a checkerboard and stripe configuration respectively. This indicates that at exactly $J_1 = 2J_2$ the model has a degeneracy and undergoes a classical phase transition from a Néel AF phase to a Stripe AF phase. Once the off-diagonal terms enter the Hamiltonian again, the states are ought to tunnel between the degenerate classical states mentioned above resulting in superpositions between the stripe configurations and between the Néel configurations for respectively $J_1 \ll J_2$ and $J_1 \gg J_2$.

Now, as mentioned in the introduction, we must first dive into the concepts of *Valence Bond States*, *Valence Bond Crystals*, before discussing the RVB states.

Let us start with the definition of a *valence bond* (VB, but also referred to as 'dimer'), which is a singlet state that connects two spins at different sites and minimizes the energy of the AF coupling between the concerning spins, such as $|0\rangle = \frac{1}{\sqrt{2}}(|\uparrow\downarrow\rangle - |\downarrow\uparrow\rangle)$. Naturally, a *Valence Bond State* is a configuration of products of VBs holding within the lattice and has total $S_{total}^2 = 0$ on even-sized lattices. Some examples of VBS configurations are

shown in figure 5.2. VBS where the dimers are not randomly placed on the lattice but are arranged in a spatially regular pattern are referred to as *Valence Bond Crystals* which can be in columnar or staggered columnar order. In order to quantify these VBS orders we define the following dimer-dimer correlators which are ought to identify dimers [37]:

$$C_d(i, j) = \langle \mathbf{B}_i^\alpha \mathbf{B}_j^\beta \rangle - \langle \mathbf{B}_i^\alpha \rangle \langle \mathbf{B}_j^\beta \rangle \quad (5.14)$$

$$= \langle (\mathbf{S}_i \cdot \mathbf{S}_{i+\alpha}) (\mathbf{S}_j \cdot \mathbf{S}_{j+\beta}) \rangle - \langle (\mathbf{S}_i \cdot \mathbf{S}_{i+\alpha}) \rangle \langle (\mathbf{S}_j \cdot \mathbf{S}_{j+\beta}) \rangle \quad (5.15)$$

$$(5.16)$$

Where $\alpha, \beta \in \{x, y\}$. The corresponding structure factor is given by:

$$S_d(\mathbf{q}) = \frac{1}{N^2} \sum_{i,j} \exp[i\mathbf{q}(\mathbf{r}_i - \mathbf{r}_j)] C_d(i, j) \quad (5.17)$$

Next to the dimer-singlet order, VBS can also exhibit longer-ranged correlations in the form of plaquettes-orders which are essentially higher order dimers which again can be in columnar or staggered columnar in a VBC and are depicted in figure 5.3.

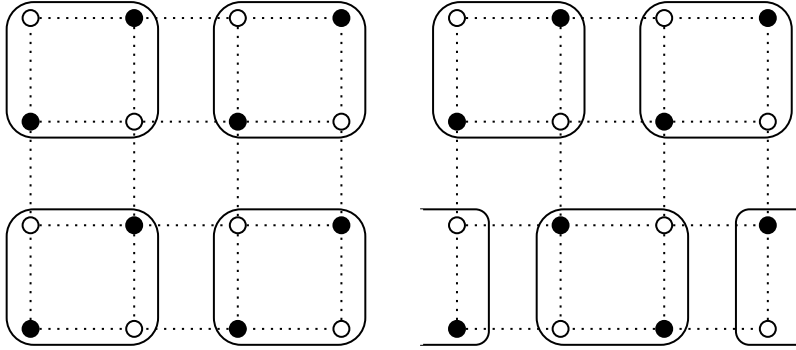


Figure 5.3: Examples of plaquettes on a 4×4 lattice. The black and white points depict the spin-up and spin-down orientations (in z-basis). From left to right: *Plaquette Bond Crystal* (PBC) and a staggered PBC

These plaquettes can be identified by the following plaquette order-parameter [16]:

$$\begin{aligned}
Q_{ijkl} &= \frac{1}{2} \left(P_{ijkl} + P_{ijkl}^{-1} \right) \\
&= 2 (\mathbf{S}_i \cdot \mathbf{S}_j \mathbf{S}_k \cdot \mathbf{S}_l + \mathbf{S}_i \cdot \mathbf{S}_l \mathbf{S}_j \cdot \mathbf{S}_k - \mathbf{S}_i \cdot \mathbf{S}_k \mathbf{S}_j \cdot \mathbf{S}_l) \\
&\quad + \frac{1}{2} (\mathbf{S}_i \cdot \mathbf{S}_j + \mathbf{S}_k \cdot \mathbf{S}_l + \mathbf{S}_i \cdot \mathbf{S}_l + \mathbf{S}_j \cdot \mathbf{S}_k) \\
&\quad + \frac{1}{2} \left(\mathbf{S}_i \cdot \mathbf{S}_k + \mathbf{S}_j \cdot \mathbf{S}_l + \frac{1}{4} \right)
\end{aligned} \tag{5.18}$$

where P_{ijkl} is a permutation operator that acts on sites i, j, k, l which together form a square on the lattice, and that cycles them in a clockwise fashion whereas P_{ijkl}^{-1} cycles counter-clockwise. With this order parameter we can define the following plaquette-plaquette correlator [16]:

$$C_p(\alpha, \beta, \gamma, \delta, i, j, k, l) = \langle Q_{\alpha\beta\gamma\delta} Q_{ijkl} \rangle - \langle Q_{\alpha\beta\gamma\delta} \rangle \langle Q_{ijkl} \rangle \tag{5.19}$$

Its structure factor is given by:

$$S_p(\mathbf{q}) = \sum_{i,j} \exp[i\mathbf{q}(\mathbf{r}_i - \mathbf{r}_j)] C_p(i, j) \tag{5.20}$$

Where in the latter equation i, j have been used to denote all sites in a plaquette and they represent the coordinates of these plaquettes. *Long range order* (LRO) in the dimer-dimer or higher order correlators such as the plaquette-plaquette correlator without spin-spin LRO are the characterisations of a VBC. Quantum fluctuations in a VBC can induce transpositions of the sites in a dimer leading to configurations that differ slightly from the initial valance bond pattern. It is essential to explain why spin $\frac{1}{2}$ excitations can not occur on a VBC (in 2D), this is because as a dimer singlet is broken into two spin $\frac{1}{2}$ objects, they perturb the ordered VBC background along a path connecting the spinons creating an effective potential that increase with the separation distance and as is depicted in figure 5.4 at a certain separation distance it will become energetically favourable to break up another bond since this has cost lower than the spin-gap, creating another two spin $\frac{1}{2}$ excitations which will together form spin 1 excitations with the former two spinons resulting in an energy of the system that is constant when the separation distance increases. This process prevents the VBC from having a single spin $\frac{1}{2}$ excitation and therefore rules out a VBC as a candidate for a QSL.

This does not change when the lattice symmetry is unbroken like in the VBS, since it also requires energy to break a singlet pair in a VBS and is

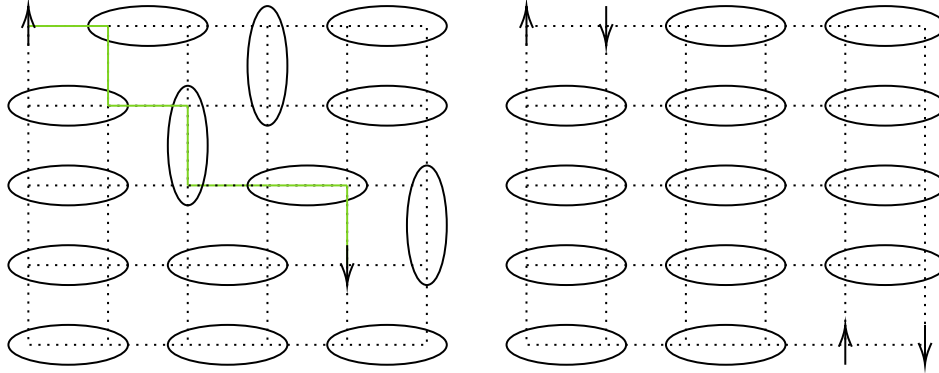


Figure 5.4: Left: excitation of a spinon separated by a distance depicted by the green line. Right: once the separation distance increases it is energetically more favourable to break another singlet bond resulting in two spin 1 excitations

therefore energetically unfavourable. Systems that are heavily effected by quantum fluctuations, however, can in fact account for tunneling between degenerate configurations. An example of such a state is the *Resonating valence bond* state that has no preferred ordering pattern and equal weight of roughly the same order of magnitude over a large part of the manifold of VBS configurations resulting in a superposition of many VBS configurations where the spin $\frac{1}{2}$ excitations might occur with possibly no energy cost induced by the quantum fluctuations as opposed to the VBC. How this relates to a QSL we will come back to later, first the formal definitions of a QSL are to be listed.

Spin Liquids

To give a somewhat brief explanation on what characterisations *do* define a spin-liquid and what type of spin-liquids (to a limited extend) exist, let us follow the definitions given in [28]. The first definition of a spin liquid is that it has *no long range magnetic order*, meaning that the spin-spin correlator $\langle \mathbf{S}_i \mathbf{S}_j \rangle$ decay to zero as $r \rightarrow \infty$. Second definition of a QSL: *A QSL is state without any spontaneously broken symmetry*. Lastly, the third definition: *A QSL is a state with fractional excitations*, which as mentioned before are usually in the form of spinons that carry half-odd-integer spin. So how does a fractional excitation arise and what does it mean? Let us first note that acting with the ladder operators S_+ and S_- in a finite number of operations can only change the total magnetization by an integer value, meaning that

creating spin $\frac{1}{2}$ excitations requires operators that act in a non-local way on the system.

Which is only expected to happen in a system of infinite size. A simple 1D example would be the spin $\frac{1}{2}$ Heisenberg chain with NN and NNN couplings at the maximally frustrated point $J_1 = 2J_2$ where the ground-states are two-fold degenerate and given by:

$$|a\rangle = \cdots \otimes |01\rangle \otimes |23\rangle \otimes \cdots \quad (5.21)$$

$$|b\rangle = \cdots \otimes |12\rangle \otimes |34\rangle \otimes \cdots \quad (5.22)$$

where the states in the tensor product consists of singlets. This is in fact a VBC where the translationial symmetry is broken spontaneously. Inserting a spin up in configuration $|a\rangle$ on , lets say, site 2 in a non local way results in a state with $S_{tot}^z = \frac{1}{2}$ where the excitation acts as a wall between $|a\rangle$ and $|b\rangle$ configurations and the excitation is a finite-energy excitation. If one acts locally with S^+ on a finite chain on site 2, another spinon is created at site 3 parallel to the spin on site 2 which can be separated to large distances with a finite energy cost and the spinons are then said to be *deconfined*. But for systems with dimension larger than one this does not necessarily hold as mentioned before concerning the 2D VBC (illustrated in 5.4). Now to describe a quantum system with these deconfined spinons one needs a formalism that includes single spinon creation and annihilation operators, which generally is done in terms of *gauge fields*. Since a spinon excitation results in a change in the magnetization by either $+\frac{1}{2}$ or $-\frac{1}{2}$, a creation of such a spinon can not be written in terms of the usual spin operators. A good start would then be to decompose the ladder operators in terms of fermionic creation and annihilation operators according to:

$$S_i^+ = c_{i\uparrow}^\dagger c_{i\downarrow} \quad (5.23)$$

$$2S_i^z = c_{i\uparrow}^\dagger c_{i\uparrow} - c_{i\downarrow}^\dagger c_{i\downarrow} \quad (5.24)$$

$$1 = c_{i\uparrow}^\dagger c_{i\uparrow} + c_{i\downarrow}^\dagger c_{i\downarrow} \quad (5.25)$$

A problem arises here since the creation operator does not transform a state to a physical state (an eigenstate of the Hamiltonian) since it is not gauge invariant. Therefore this requires some form of information of the path a spinon can travel encoded in the operator, which will be accounted for by the gauge field. It is known that both physical states and spin operators are invariant under the following transformation:

$$c_{i\sigma}^\dagger \rightarrow \exp(-i\Delta_i) c_{i\sigma}^\dagger \quad (5.26)$$

where $\sigma \in \{\uparrow, \downarrow\}$ and $\Delta_i \in [0, 2\pi[$. Now to make the creation operator transform physical states into physical states a gauge field A_{ij} is introduced that transforms as $A_{ij} \rightarrow A_{ij} + \Delta_i - \Delta_j$ so that change in phases is accounted for and leaves the term $c_{i\uparrow}^\dagger c_{i\downarrow}$ gauge invariant since $c_{0\uparrow}^\dagger \exp(A_{01} + \dots + A_{n-1}) c_{n\uparrow}$ is gauge invariant under the transformation rule mentioned before. These gauge fields are used to describe the type of spin liquid in question. A \mathbb{Z}_2 spin liquid for instance can only have angular values of either 0 or π whereas a $U(1)$ spin liquid can have any angular value in the range $[0, 2\pi[$.

Coming back to the absence of a magnetic order in QSLs it is worth mentioning that a form of *order* is generally caused by spontaneous symmetry breaking process and translates into having multiple ground-states that are degenerate as $L \rightarrow \infty$. Distinguishing these ground-states can then be done by calculating the expectation values of an observable acting on these states. If this observable is able to distinguish these states it is referred to as an *order-parameter* of the broken symmetry. If, however, the lattice has a topology that is non trivial, as it is for tori and cylinders, a QSL with fractionalization will have a ground-state degeneracy despite the absence of a broken symmetry. This means that it exhibits an order that can not be measured using an order-parameter but is related to its topology and is therefore referred to as *topological order*[52, 54, 53]. To illustrate this let us consider the following example where we start with a state where a pair of spinons is created on a cylinder, which is called state $|0\rangle$ and is acted upon with an unitary operator \mathcal{R} that moves one of the spinons around to the cylinder such that $\mathcal{R}|0\rangle = |1\rangle$ and takes the spinon back to where the original pair was formed only to be annihilated again. This could result in the original state we started with but it does not necessarily have to be that state. During the process of moving a spinon the intermediate states can be viewed as states without spinons but where the spinons are connected along a path/string via the gauge-fields, which, after the annihilation of spinons when they meet again, remains and is non contractible and hence distinguishes the original state from the new state due the topology of the system. At the end of the previous section the RVB was mentioned as a possible SQL candidate, let us therefore briefly elaborate how the RVB relates to a QSL. Starting with a RVB wave function $|\varphi\rangle = \sum_a \phi(a) |a\rangle$ where a denotes the configuration of valence-bonds on the lattice and $\phi(a)$ denote the corresponding weights. If then $|\varphi\rangle$ is a description for a RVB liquid then it must have no configuration to compare to, in other words it should not have a parent configuration from where it could arise, yet it can still transition to another configuration by creating a spinon pair of which a spinon can prop-

agate along some closed loop to annihilate again by forming a (short range) valence bond in the other configuration. The latter process is referred as *resonating loop*, and the size of such loops represents the distance between these excited spinons and differs for short-range and long-range RVBs. In the former RVB the loops are large whereas in the latter RVB the loops are small. Lastly, determining whether a spin-liquid is gapped or not depends on the behaviour of the Hamiltonian in the large L limit, more specifically: in order to find out whether the spinon excitations are gapped or gapless, one needs to calculate the singlet and triplet gaps and see if it closes as L increases. There are more types of spin-liquids worth mentioning and there have been extensive studies aimed to find the nature of ground-state around $J_1 = 2J_2$ of which some indicate a gapped spin-liquid [23], others a gapless spin-liquid [50, 33, 22], and VBC orders [59, 34, 18]. Since the explanation here is meant to be brief I suggest the reader to read [29, 28] for a more elaborate explanation on QSLs.

So what does this mean for the TTN ansatz, and how can a TTN distinguish between these orders? Well it is interesting to find out to what extend a TTN can cover the physical properties of the $J_1 - J_2$ spin $\frac{1}{2}$ Heisenberg model around the maximally frustrated point $J_1 = 2J_2$, by calculating the correlators introduced before, and check whether the definitions of a spin-liquid mentioned earlier apply to the found ground-states. It should be noted that using finite lattices forces us to look at the maximum distance correlators for increasingly larger lattices in order to get an understanding of what orders occur in the thermodynamic limit.

Chapter 6

Results & discussion

6.1 Introduction

The following sections are split into parts concerning 1D and 2D results for the Transverse Field Ising model followed by 2D results for the J_1 - J_2 Heisenberg model. For the Transverse Field Ising model ground-state energies are presented along with the scalings of the relative-error with respect to the exact ground-state energy, the iteration time, and the entanglement entropies as functions of the bond-dimension. For the *1D* TFI model spin- $\frac{1}{2}$ chains of linear size $L \in \{8, 16, 24, 32\}$ are considered, whereas for the *2D* Transverse Field Ising model spin- $\frac{1}{2}$ lattices of linear size $L \in \{4, 6, 8\}$ are considered.

The Heisenberg $J_1 - J_2$ model on lattices of linear sizes $L = 4$ and $L = 8$ is studied in more detail as first next to the ground-state energies, entanglement entropies, and the relative errors the phase diagram is studied in more detail using the correlators defined in section 5.3 in an attempt to find the ground-state orders. For both models periodic boundary conditions are used.

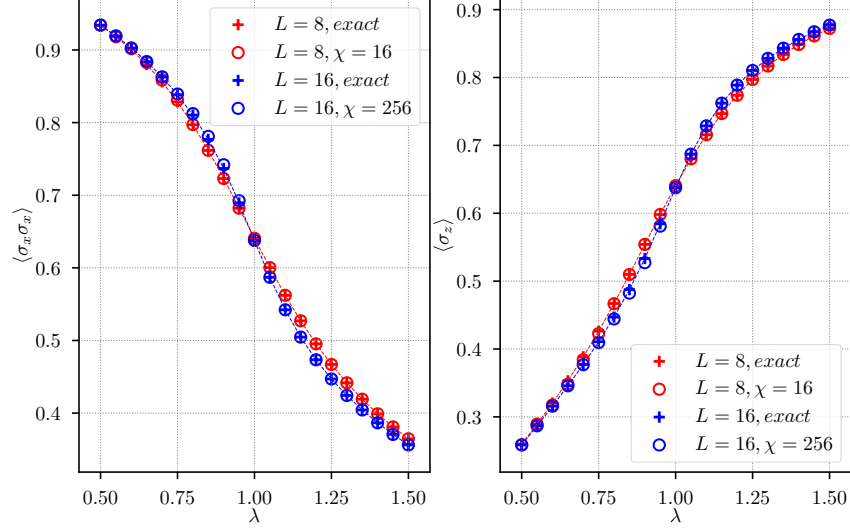


Figure 6.1: Left the expectation value $\langle \sigma_x \sigma_x \rangle$, and right the expectation value $\langle \sigma_z \rangle$ which are both calculated for 1D systems of sizes $L \in \{8, 16\}$ and compared the exact diagonalization results.

6.2 Transverse Field Ising: 1D

6.2.1 Ground-state energy

In order to depict the ground-state simulations done let us start by introducing the ground-state energy per site which is defined in terms of the following expectation values. The first term:

$$\langle \sigma_x \sigma_x \rangle \equiv \frac{1}{N} \sum_{\langle i, i+1 \rangle} \langle \sigma_x^i \sigma_x^{i+1} \rangle \quad (6.1)$$

and the transverse magnetization:

$$\langle \sigma_z \rangle \equiv \frac{1}{N} \sum_i \langle \sigma_z^i \rangle \quad (6.2)$$

Both of which are presented in figure 6.1 along with the exact values for L up to (including) 16, which clearly shows the overlap of the exact diagonalization results with the TTN results although they differ more in the vicinity

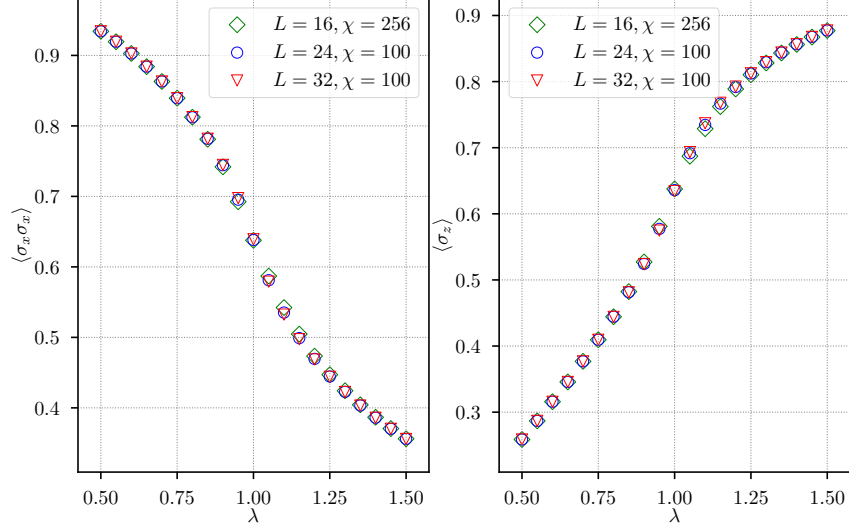


Figure 6.2: Left the expectation value $\langle \sigma_x \sigma_x \rangle$, and right the expectation value $\langle \sigma_z \rangle$ which are both calculated for 1D systems of sizes $L \in \{16, 24, 32\}$.

of the λ_c which is expected since faithfully representing the ground-state in this region is more difficult.

The expectation values of equations 6.1 and 6.2 for $L \geq 16$ are depicted in figure 6.2. Since the computational power did not allow for exact diagonalization of systems of $L \geq 32$ the results for the largest bond-dimension used are shown ($\chi = 100$). The energy per site is defined as a combination of the above expectation values according to:

$$e = \frac{1}{N} \langle H \rangle = \langle \sigma_x \sigma_x \rangle - \lambda \langle \sigma_z \rangle \quad (6.3)$$

Which is used to define the error as a function of the bond-dimension $\Delta e(\chi)$. However, since for system sizes larger than linear size L of 16 exact diagonalization was not an option, the error for $L \in \{24, 32\}$ is obtained via the relative error with respect to the largest bond-dimension. In other words for L up to 16 the exact error is defined as:

$$\Delta e(\chi) \equiv |e_{exact} - e(\chi)| \quad (6.4)$$

And for $L > 16$ this becomes the relative error:

$$\Delta e(\chi) \equiv |e_{\chi_{max}} - e(\chi)| \quad (6.5)$$

The errors are depicted in figure 6.3 and are of the same order of machine-

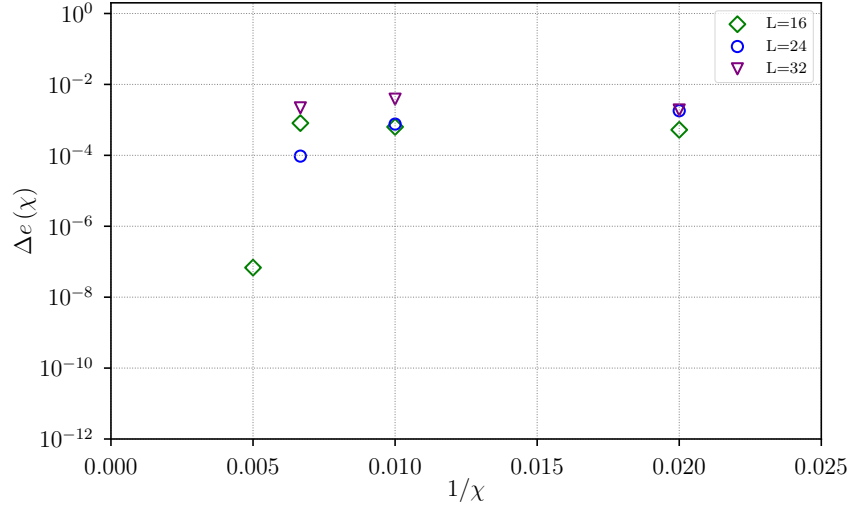


Figure 6.3: The error in the ground-state energy as a function of the bond-dimension at λ_c . Notice that for the smaller system with $L = 16$ the error rapidly decreases as χ reaches its exact value yet for the larger systems the errors decrease significantly slower. The increment in the errors is caused by the systems that have not fully converged to their final values yet since the maximum amount of iterations is kept to 600.

precision for $L = 16$ whilst for $L > 16$ higher values of χ should be considered in order to obtain accurate ground-state energy results.

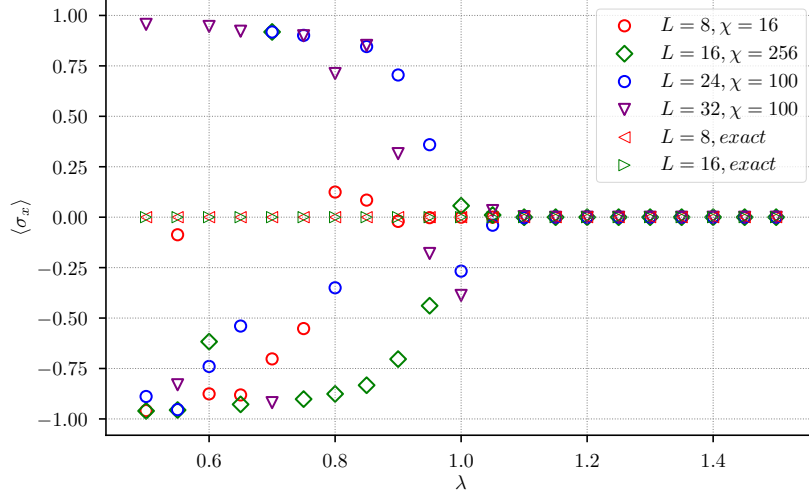


Figure 6.4: 1D magnetization $\langle \sigma_x \rangle$ for systems of sizes $L \in \{8, 16, 24, 32\}$ along with the exact results for $L = 8$ and $L = 16$.

6.2.2 Magnetization

As mentioned in section 5.2, we expect for finite systems that the magnetization is zero. However figure 6.4 clearly shows differences for the smaller 1D systems compared to their exact versions, from which we can conclude that the finite bond-dimension along with the possibility that full convergence has not been reached yet can lead to the states being close to symmetric degenerate state yet ending up in a magnetized state, which in turn can lead to non zero magnetizations for systems in the region that is ought to be the ordered phase. Once λ exceeds λ_c , which is shifted to smaller values of λ for finite systems, the magnetization does vanish as is expected in the disordered phase.

6.2.3 Entanglement entropy

In the classical limit where $\lambda = 0$, the entanglement entropy is close to 0.7 since the ground-state consists of two states with either all spins pointing upwards or downwards resulting in $S = \log 2 \approx 0.7$. As λ increases we expect the entanglement entropy to increase as the ground-state becomes more entangled, reaching its maximum at λ_c , yet figure 6.5 shows a different

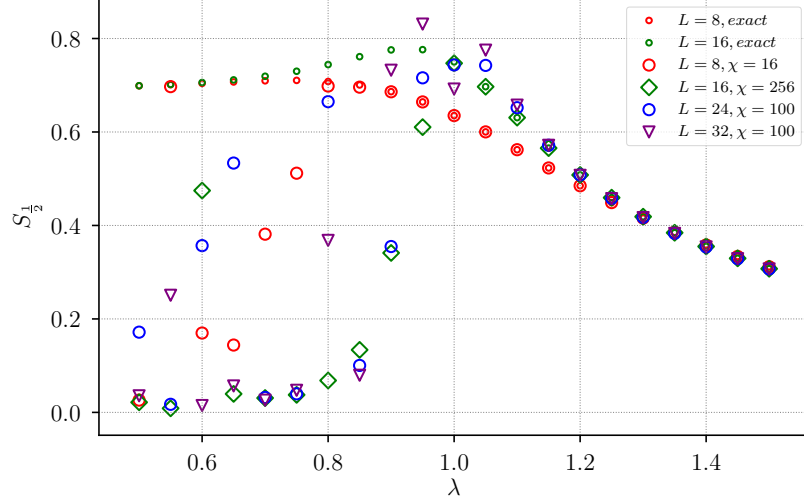


Figure 6.5: Entanglement entropy for L up to 32. For $L = 8$ and $L = 16$ it is compared to the exact ground-state entanglement entropy

picture. Although the results in the vicinity of λ_c and upwards seem to be very accurate for the smaller systems where they are compared to the exact results, the TTN does struggle to faithfully represent ground-states in the ordered phase ($\lambda < \lambda_c$) which follows an identical explanation as for the non-zero magnetization from figure 6.4 where both the finite bond-dimension and poor convergence can lead to states ending up in a magnetized state since for finite values of λ the gap between the ground-states and the first excited states (energy differences) can be small.

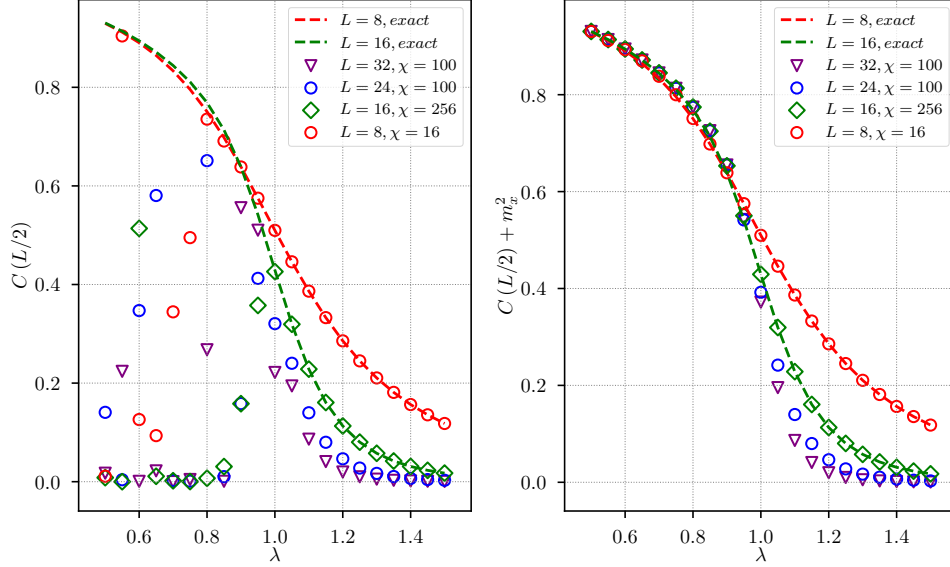


Figure 6.6: $C(L/2)$ for systems of size $L \in \{8, 16, 24, 32\}$ along with the exact diagonalization results for $L = 8$ and $L = 16$. Since the magnetization is found to be non-zero using the TTN ansatz both $C(L/2)$ (left) and $C(L/2) + m_x^2$ (right) are shown

6.2.4 Correlation functions

As mentioned in section 5.2 it is instructive to study the behaviour of the maximum distance correlators as a function of λ for lattices of increasing size L and compare these to their corresponding exact diagonalization versions to study the behaviour in the thermodynamic limit. Both the correlators and the exact diagonalization results are shown in figure 6.6. Note that when the magnetization is omitted the correlator does not seem to differ from the exact results. Furthermore it is worth mentioning that as the system size grows, the curve becomes increasingly sharper around λ_c , indicating that the phase transition in the thermodynamic limit does occur at $\lambda = 1.0$. Since the structure of the TTN manifestly breaks translation invariance, it is interesting to further investigate how this affects the correlators. Let us therefore look at the correlators as a function of the distance, x , namely

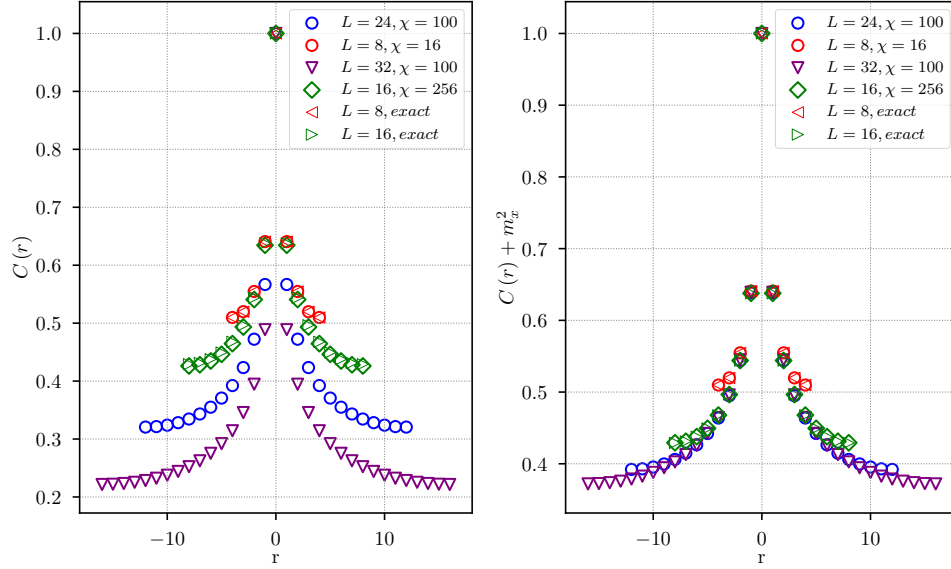


Figure 6.7: $C(x)$ for systems of size $L \in \{8, 16, 24, 32\}$ at $\lambda = 1.0$ compared to the exact results for $L = 8$ and $L = 16$. Left: $C(x)$ with correction for the magnetization, equation 6.6. Right: $C(x)$ without correction for the magnetization, equation 6.7.

spin-spin correlator for σ_x , as follows:

$$C(x) \equiv \langle \sigma_x^0 \sigma_x^x \rangle - \langle \sigma_x^0 \rangle \langle \sigma_x^x \rangle \quad (6.6)$$

$$= \langle \sigma_x^0 \sigma_x^x \rangle \quad (6.7)$$

where the last term $\langle \sigma_x^0 \rangle \langle \sigma_x^x \rangle$ has been omitted since they yield non-zero magnetizations. These correlators are depicted in figure 6.7 for $\lambda_c = 1.0$. Note that the correlators do not seem to suffer from the structure of the TTN as they are near identical in both directions, $C(-x) \approx C(x)$.

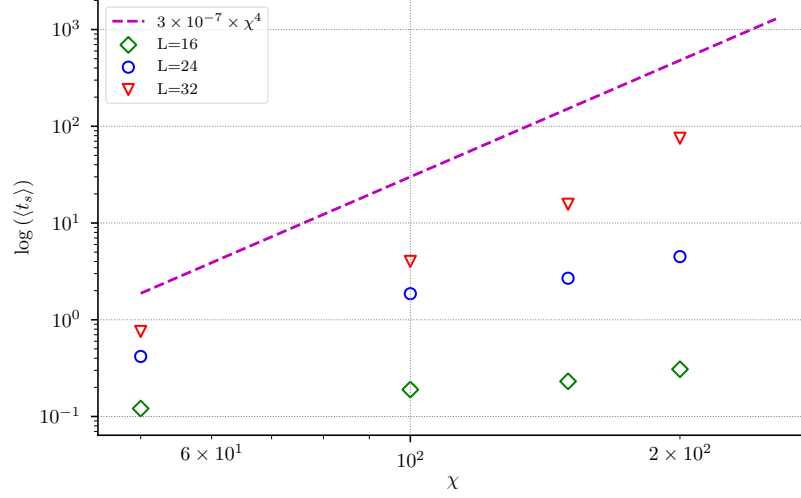


Figure 6.8: Iteration time per sweep at λ_c for systems of size $L \in \{16, 24, 32\}$

6.2.5 Iteration time scaling and convergence

Let us now look at the mean iteration time per sweep near λ_c : $\langle t_s \rangle$ which are shown in figure 6.8. Recall that the expectation of the scaling of the iteration time was of the order $\mathcal{O}(L\chi^4)$ as explained in section 4.2.3 yet this is far from the observed scaling, which is due to χ not being large enough to show this scaling.

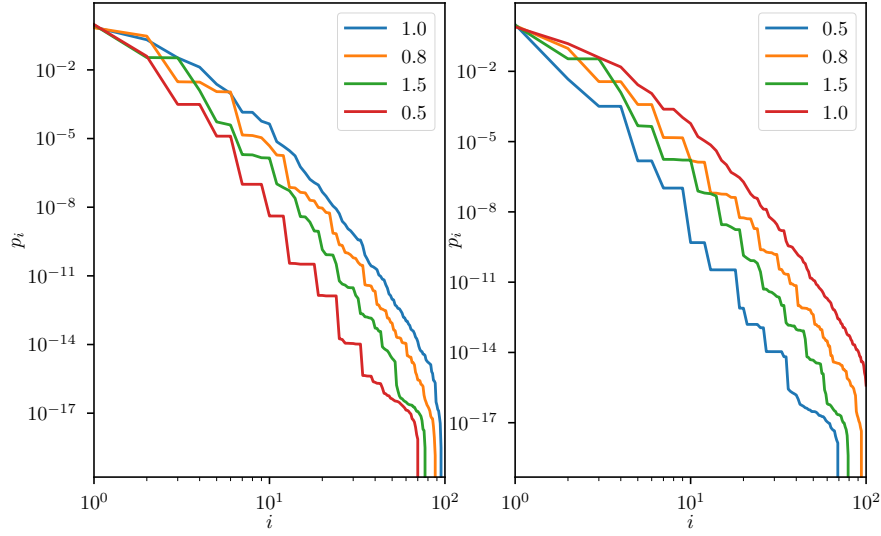


Figure 6.9: Spectrum of eigenvalues of the reduced density matrix ρ_A of one half of the system of size $L = 24$ in the left figure and $L = 32$ in the right figure, and with $\chi = 100$, and different values of λ

Another way of identifying convergence is to look at the spectrum of eigenvalues of one half of the system, p_i , which should decay very rapidly if convergence has been reached. As figure 6.9 shows, near λ_c the ground-state is most entangled, and therefore its computation most challenging, resulting in turn to a slower decay of the eigenvalues compared to other values of λ .

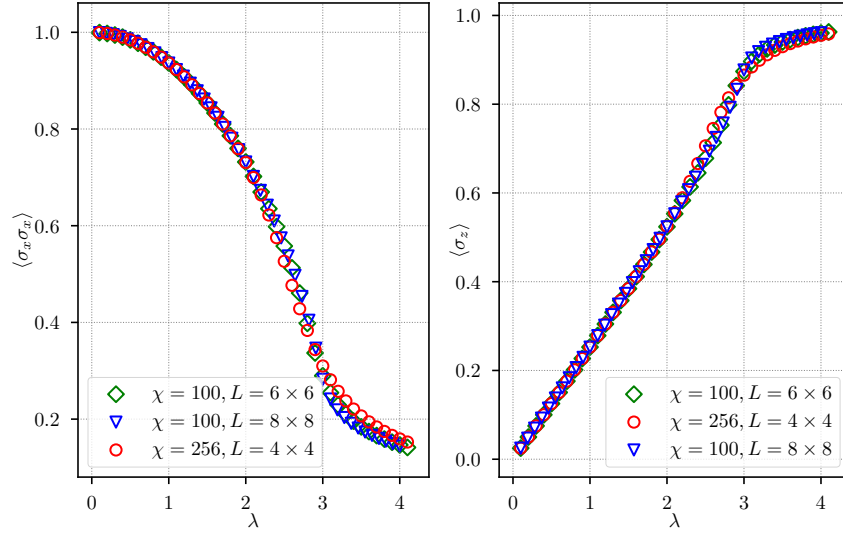


Figure 6.10: Left: mean interaction per link $\langle \sigma_x \sigma_x \rangle$. Right: transverse magnetization per site $\langle \sigma_z \rangle$. Notice the transitions of are increasingly sharper as the system size grows with L .

6.3 Transverse Field Ising: 2D

6.3.1 Ground-state energy

The ground-state simulations done with the TTN ansatz are for 2D system sizes are of linear size $L \in \{4, 6, 8\}$ and are illustrated in figure 6.10, where the following expectation values are plotted:

The interaction per link:

$$\langle \sigma_x \sigma_x \rangle \equiv \frac{1}{2N} \sum_{\langle i, j \rangle} \langle \sigma_x^i \sigma_x^j \rangle \quad (6.8)$$

And the transverse magnetization:

$$\langle \sigma_z \rangle \equiv \frac{1}{N} \sum_i \langle \sigma_z^i \rangle \quad (6.9)$$

Then the energy per site in terms of these expectation values is:

$$e \equiv \frac{1}{N} \langle H \rangle = -2 \langle \sigma_x \sigma_x \rangle - \lambda \langle \sigma_z \rangle \quad (6.10)$$

Similarly to the 1D results the relative -and exact errors of equations 6.4 and 6.5 are used for systems with square size $L > 4$.

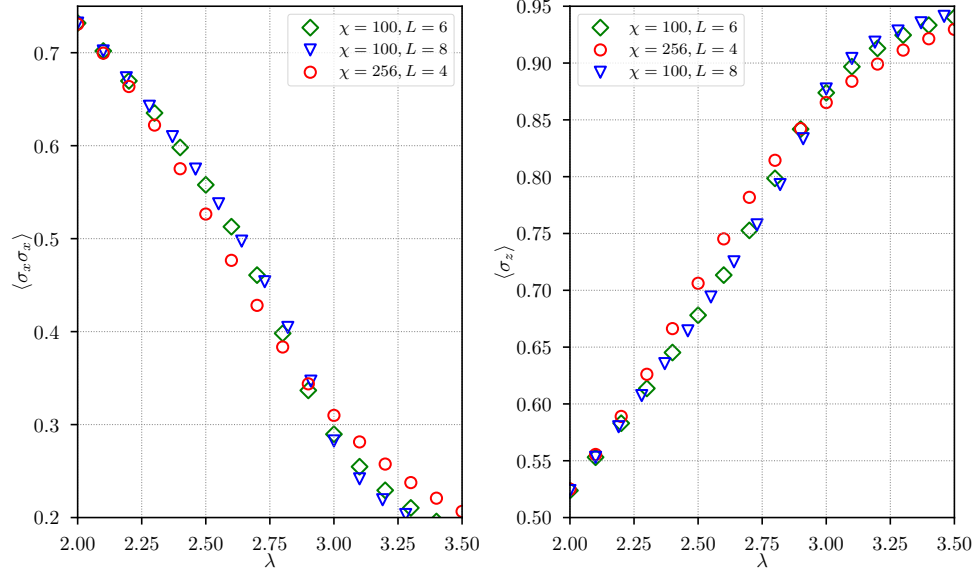


Figure 6.11: Zoomed in versions of the expectation values $\langle \sigma_x \sigma_x \rangle$ and $\langle \sigma_z \rangle$ shown in figure 6.10.

As mentioned in figure 6.10 the curves of the expectation values are increasingly sharper for growing L . This behaviour is illustrated in more detail in figure 6.11. However, much insight on the exact location of λ_c can not be drawn from the mean interaction per link and must be obtained by looking at the behaviour of the maximum distance correlators.

As for the ground-state energy per site error for the 2D TFI both equation 6.4 and 6.5 are used to determine the exact and relative errors as function of χ respectively and are depicted in figure 6.12 at $\lambda = 3.0$. For the 4×4 lattice the error is of the order of machine precision at the largest possible bond-dimension, namely $\chi = 256$. For the larger lattices (6×6 , 8×8) the results are obtained via the relative error by comparing the ground-state energies to the ground-state energies for $\chi = 200$.

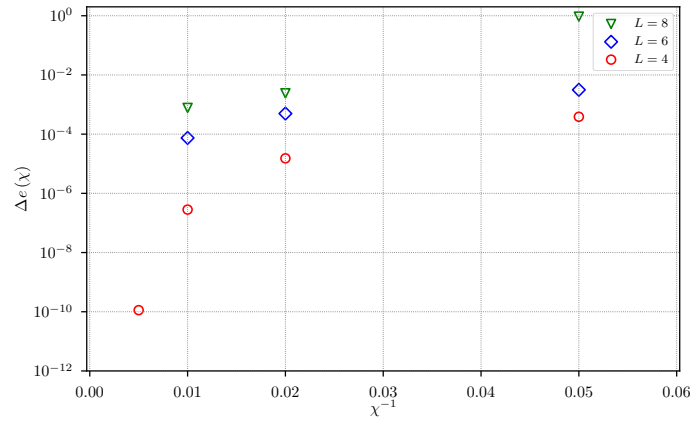


Figure 6.12: The error in the ground-state energy as a function of the bond dimension at $\lambda \approx \lambda_c = 3.0$.

It is worth mentioning that using $\chi = 100$ for latter lattices of already result in significantly small errors.

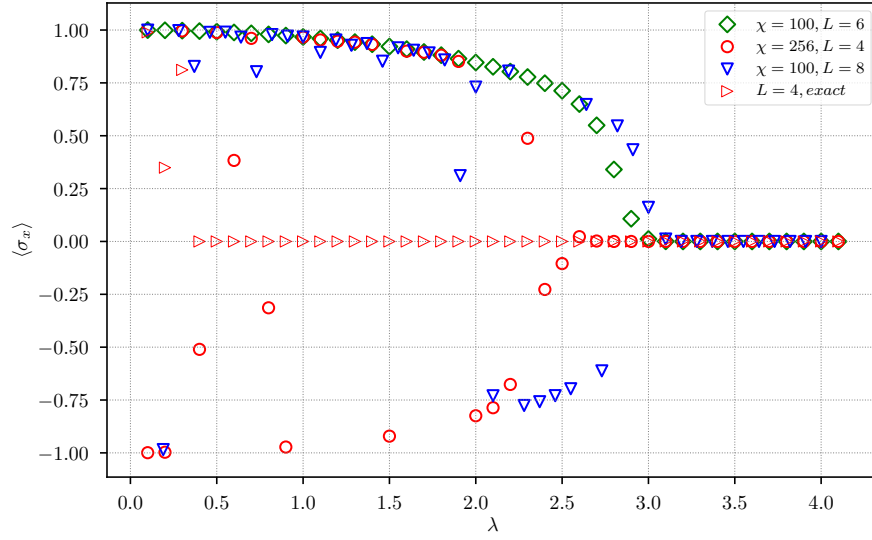


Figure 6.13: $m_x \equiv \langle \sigma_x \rangle$ for systems of size $L \in \{4, 6, 8\}$

6.3.2 Magnetization

Similarly to the 1D case, where the magnetization is found to be non-zero as discussed in section 6.2.2, the 2D systems also seem to have non-zero magnetizations, as illustrated in figure 6.13. Which, again, is caused by the usage of a finite- χ , given the exact diagonalization results yield zero magnetization.

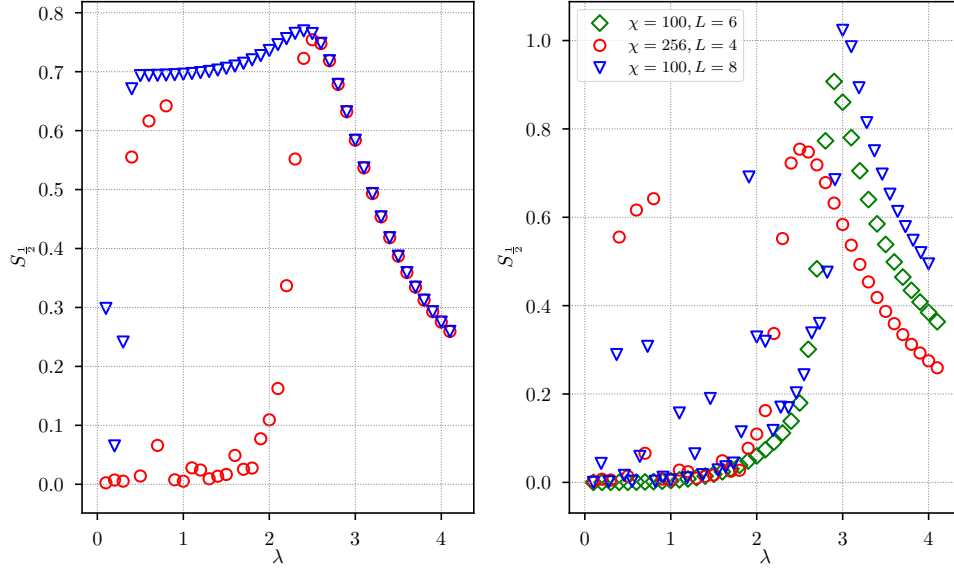


Figure 6.14: Entanglement entropy for a half of the system, $S_{\frac{1}{2}}$, for the exact ground-state and for the TTN approximation for the highest possible χ . Left $S_{\frac{1}{2}}$ for the 4×4 lattice compared to the exact diagonalization results. Right: $S_{\frac{1}{2}}$ for the 4×4 , 6×6 , and 8×8 lattices.

6.3.3 Entanglement entropy

For the systems at the critical point $\lambda \approx 3$ the entanglement entropy should be the highest, yet for the 4×4 system where an exact comparison can be made it is found that the TTN ansatz fails to faithfully describe this as the entanglement entropy remains significantly low away from λ_c as is shown in figure 6.14. This follows an identical explanation as for the 1D case, since we expect the entropy to be close to $\log 2$ at $\lambda = 0$ and to increase as λ increases, reaching its maximum at λ_c , yet the usage of a finite χ can cause the TTN to not faithfully represent the ground-state. For $L > 4$ there is no comparison available to the entanglement entropy of the exact ground-state, nevertheless the entanglement entropy behaves almost identical to that of the 4×4 system, as illustrated in right plot of figure 6.14 where it is also clear that the finite size of the systems causes the λ_c to shift to be smeared out over a range of λ although they seem to converge to the λ_c in the thermodynamic limit ($L \rightarrow \infty$).

6.3.4 Correlation functions

Since the TTN ansatz breaks translational symmetry it is instructive to see whether, and if so how, this affects the correlation functions near criticality. First let us define the correlation functions of interest.

$$C(x, y) \equiv \langle \sigma_x^{[0,0]} \sigma_x^{[x,y]} \rangle - \langle \sigma_x^{[0,0]} \rangle \langle \sigma_x^{[x,y]} \rangle \quad (6.11)$$

$$= \langle \sigma_x^{[0,0]} \sigma_x^{[x,y]} \rangle \quad (6.12)$$

Where the contribution of $\langle \sigma_x^{[0,0]} \rangle \langle \sigma_x^{[x,y]} \rangle$ is neglected due to the non-zero magnetizations as depicted in 6.13. As figure 6.15 shows, the rotational

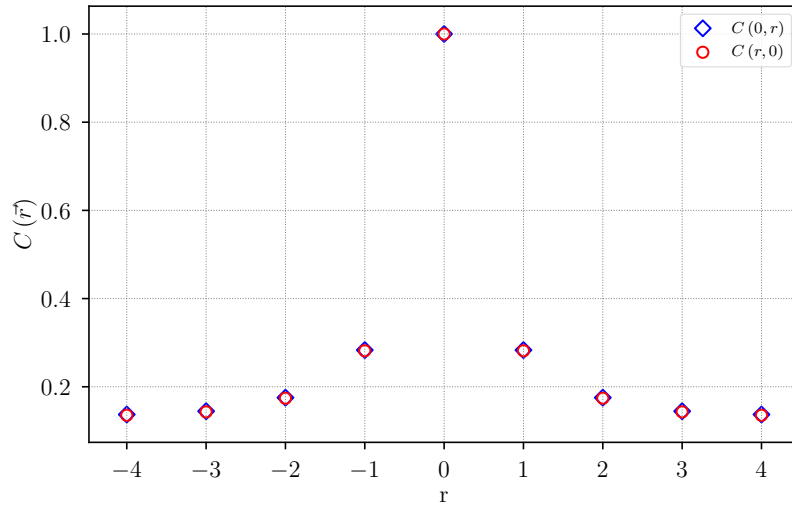


Figure 6.15: spin-spin correlation functions for σ_x in the x ($C(r, 0)$) and the y ($C(0, r)$) directions for the 8×8 lattice for $\lambda = 3$

invariance already seems to be restored for a $\chi = 100$ at λ_c . Furthermore, as shown in figure 6.18 at this λ_c the eigenvalues have not converged fully yet, indicating that the TTN ansatz does not suffer from spatial symmetries being broken at criticality as it does not in the 1D case. Let us now look at the long distance correlators as depicted in figure 6.16, where in the long distance correlator in the x direction is shown in the left plot and in the y direction in the right plot. As the system size increases the curve becomes increasingly sharper

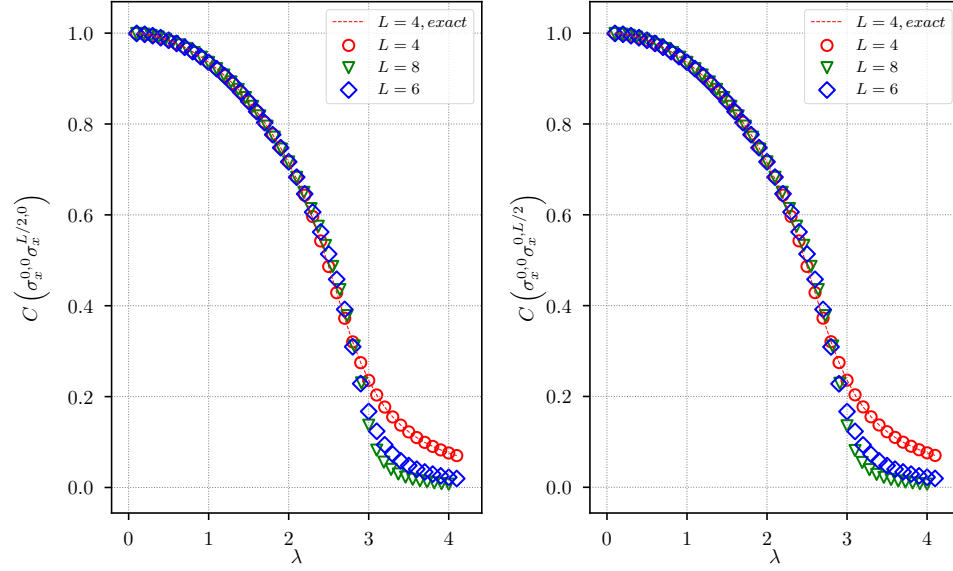


Figure 6.16: Left: spin-spin correlator of $\langle \sigma_x^{r=0} \sigma_x^{r=L/2} \rangle$ in the x -direction. Right: spin-spin correlator of $\langle \sigma_x^{r=0} \sigma_x^{r=L/2} \rangle$ in the y -direction.

6.3.5 Iteration time scaling and convergence

The scalings for the mean iterations times per sweep near λ_c are shown in figure 6.17 together with the function $3 \times 10^{-7} \times \chi^4$, in order to compare to the expected scaling. Again, similar to the 1D case, the iteration times do not scale as the scaling of the cost $\mathcal{O}(\chi^4)$.

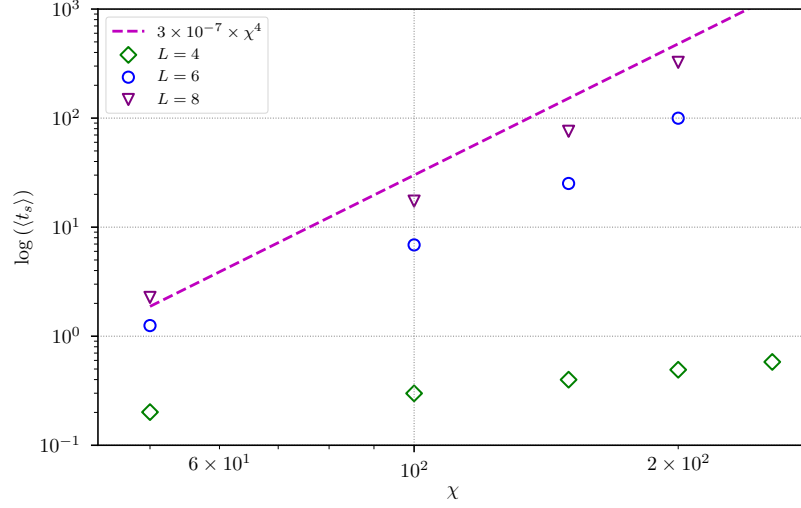


Figure 6.17: Mean iteration time per sweep near $\lambda_{critica} \approx 3$ for 2D systems, $\langle t_s \rangle$ as a function of the bond-dimension

To study the convergence of the simulations it is instructive to look at the spectrum of eigenvalues of the reduced density matrix of one half of the system, p_i which for the largest system of size $L = 8$ and $\chi = 100$ is displayed in figure 6.18. Away from λ_c we expect the eigenvalues to decay fast, whereas near λ_c we expect the eigenvalues to decay significantly slower as it becomes harder to represent the ground-state. This behaviour of p_i is confirmed in figure 6.18.

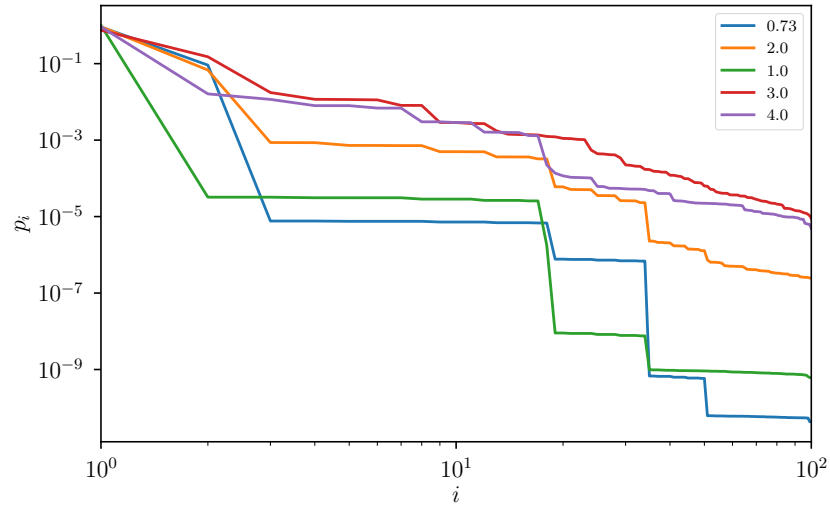


Figure 6.18: Spectrum of eigenvalues of the reduced density matrix of block A (ρ_A), p_i for multiple values of λ

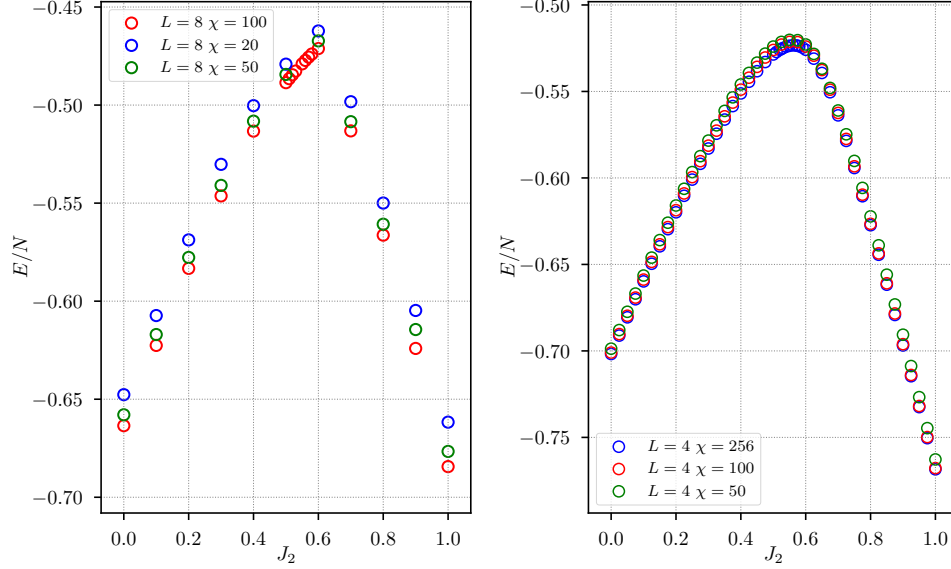


Figure 6.19: Left: Energy per site $e \equiv E_{total}/N$ for a 8×8 lattice with bond dimensions $\chi \in \{20, 50, 100\}$. Right: Energy per site E/N as a function of J_2 for the 4×4 lattice and different values of the bond-dimension

6.4 J_1 – J_2 Heisenberg model

6.4.1 Ground-state energies

The simulations for the J_1 – J_2 Heisenberg model are performed on lattices of linear sizes $L = 4$ and $L = 8$. The $N = 4 \times 4$ results are obtained by means of a triple layer TTN, whereas the $N = 8 \times 8$ results are obtained via a quadruple layer TTN, meaning that the bottom layer consists of rectangular lattices instead of square lattices which is an important detail for later discussion. The linear sizes are a multiple of 2 to facilitate possible dimer or plaquette orderings on the lattices, which are harder to form on lattices whose linear sizes are not a multiple of 2. Another important note is that like for the 1D and 2D TFI translational symmetry is used by choosing every isometry in the bottom layer to be the same. Whether this might or might not affect the possible orders formed on the lattice will be discussed in section 6.4.3 on the correlation functions. Furthermore for all simulations J_1 is set to 1 for simplicity.

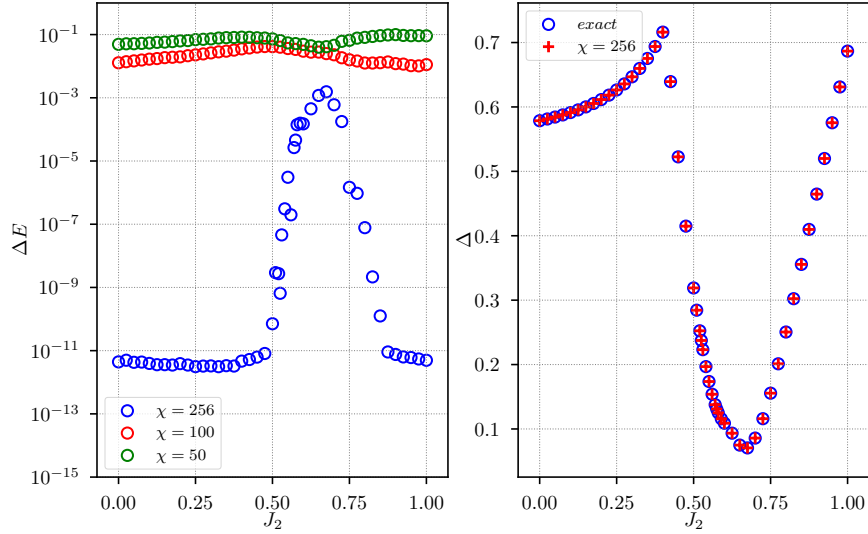


Figure 6.20: Left: Exact error Δe from equation 6.4, for the 4×4 lattice. Right: Energy gap between the ground-state and the first excited state Δ compared to the gap obtained by exact diagonalization.

Let us first look at the effect of the bond-dimension to the energies per site, which are shown in figure 6.19. Left are the energies per site for the 4×4 lattice, and on the right for the 8×8 lattice. As expected, a higher bond-dimension leads to higher energies for the $J_1 - J_2$ Heisenberg model, since it determines the amount of states kept and less states kept leads to less positive corrections to the ground-state energies per site. For the errors let us start by looking at the results for the ground-state energies along with the errors defined by equations 6.4 and 6.5, more specifically let us look at $J_2 = 0$ for the 4×4 lattice where a comparison to results in the literature is available. The exact diagonalization results obtained are identical to the results obtained from an exact diagonalization study [41] for all values of J_2 that are considered. It is interesting to mention that the error increases significantly in the region $0.5 < J_2 < 0.8$ depicted in the left plot of figure 6.20, whereas outside this region the error is of the same order as machine precision. Looking at the entanglement entropy of one half of the system in the left plot of figure 6.21, we can see that the entropy also increases as it reaches its maximum around the value where the error also has its

J_2	$L = 4 \text{ TPS}$	$L = 4 \text{ exact}$	$L = 4 \text{ TTN}$	$L = 8 \text{ TPS}$	$L = 8 \text{ TTN}$
0.50	-0.5268	-0.528620	-0.528620	-0.4984	-0.4886
0.52	-0.5227	-0.525938	-0.525938	-0.4941	-0.4846
0.55	-0.5192	-0.523594	-0.523594	-0.4880	-0.4790
0.60	-0.5177	-0.525896	-0.525886	-0.4808	-0.4712

maximum (for the largest bond-dimension). This increase in entanglement entropy might suggest, as it also had its maximum around λ_c in the 1 -and 2D TFI, the presence of a critical point. The right plot of figure 6.20 also suggests a critical point as the gap between the ground-state and the first excited state reaches its minimum near $J_2 = 0.6$. We expect that this gap in the Neel and Stripe phase closes as $L \rightarrow \infty$ yet for the intermediate QSL phase it is still not clear whether this gap closes. We will come back to determining the order of the ground-states in the section on the correlation functions, for now let us continue and compare the energies per site within the region $0.5 \leq J_2 \leq 0.6$ to a study that employed *Tensor Product States* [49] to determine the phase diagram and the ground-state energies. These results in table 6.4.1 show that the TTN outperforms the TPS on the 4×4 lattice, despite the increasing error for these values of J_2 .

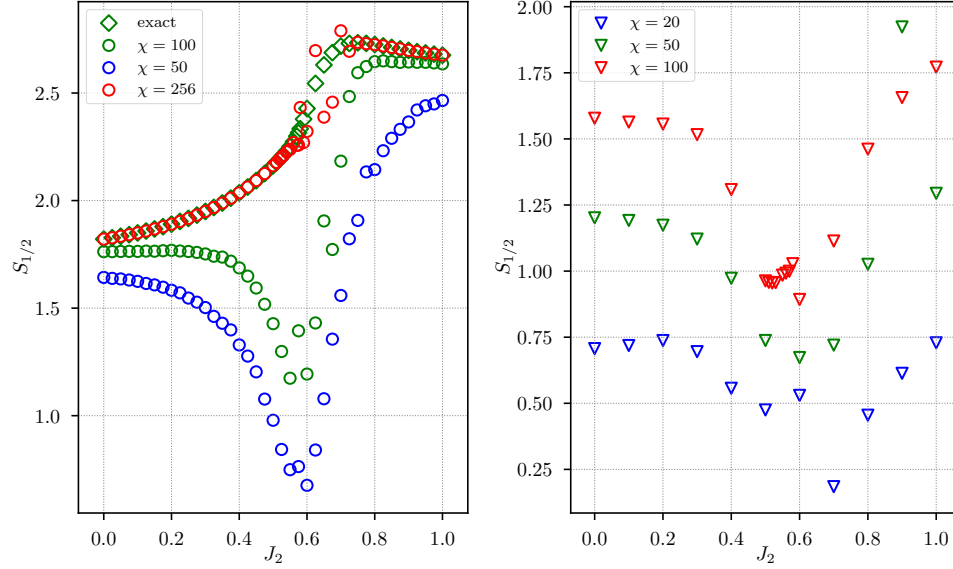


Figure 6.21: Left: entanglement entropy $S_{1/2}$ for 4×4 lattice for $\chi \in \{50, 100, 256\}$ compared to the exact ground-state entanglement entropy. Right: entanglement entropy $S_{1/2}$ for the 8×8 lattice for $\chi \in \{20, 50, 100\}$

6.4.2 Entanglement entropy

Figure 6.21 shows the entanglement entropies of both the 4×4 (left) and the 8×8 (right) lattice for different values of χ . The left plot clearly shows that a relatively high value of χ is required to get near the exact results since the values of $\chi < 256$ result in failing to capture the increase in $S_{1/2}$ which is expected to occur as the system becomes more frustrated. A similar decrease is also obtained from the simulations of the 8×8 lattice where the exact value of χ , that is $\chi = 2^{32}$, is impossible to implement due to the computational costs. Nevertheless, the similar behaviour of these truncated values of χ to those of the 4×4 lattice suggest that in the exact χ limit these decreases will most likely vanish, as they do for the exact χ of the 4×4 lattice.

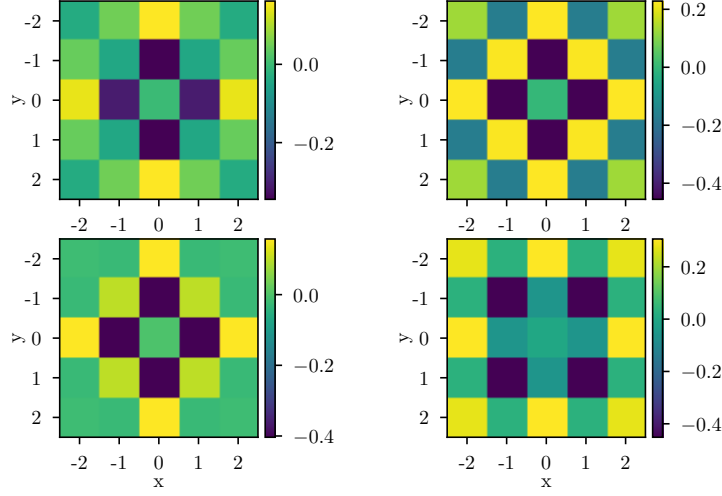


Figure 6.22: All correlators for the 4×4 lattice with $\chi = 256$, and J_2/J_1 being from top left to bottom right: 0.58, 0.325, 0.5, 0.8 calculated on a 5×5 lattice

6.4.3 Correlation functions

As mentioned in section 5.3 Contrary to the correlators used for the Transverse Field Ising model, the correlators used for the J_1 - J_2 model are chosen differently. This is due to the pattern that the correlators have in the ground-states of different phases. As mentioned in section 6.4.1 the model exhibits multiple phases, of which the AF phase has a checkerboard pattern and the Stripe phase a stripe pattern. The correlator from equation 5.12 for distances up to $L/2$ for the 4×4 lattice is shown in figure 6.22 for different values of J_2 . For $J_2 = 0.325$ we can still see a clear Néel AF pattern and for $J_2 = 0.8$ we can see a clear stacked pattern of both horizontal and vertical stripes, which was expected to happen for $J_2 > J_1$. In the vicinity of $J_1 = 2J_2$ the correlations seem to be short ranged, although the max distance correlators remain non-zero, which is expected to occur on finite lattices.

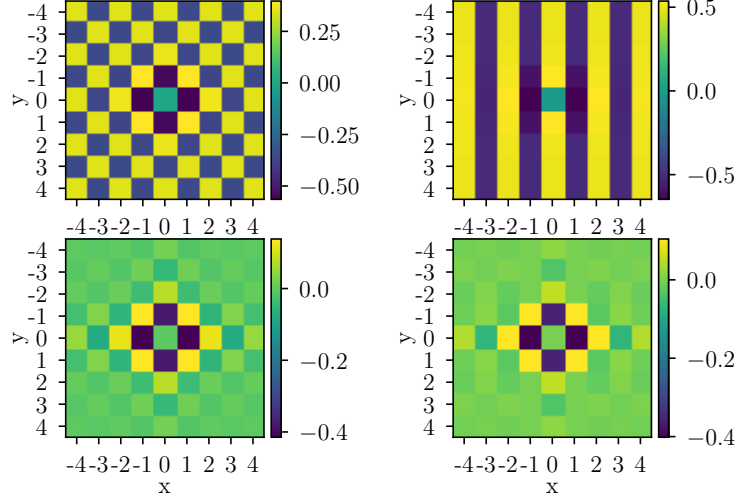


Figure 6.23: All correlators for the 8×8 lattice with $\chi = 100$, and J_2/J_1 being from top left to bottom right: 0.3, 0.8, 0.5, 0.58 calculated on a 9×9 lattice

As mentioned in the previous section on the entanglement entropies, the entanglement entropy for the 8×8 lattice is expected to be higher than the results for the largest bond-dimension used. This can be an indication that the resulting correlators might not represent the proper ground-state but instead a portion of the configurations of the ground-state. For example, not being able to show the stacked stripes as the correlators for the 4×4 did show. In figure 6.23 these correlators are shown for different values of J_2 . As expected, we only find the vertical stripe pattern for $J_2 = 0.8$, which is the result of having a relatively small χ compared to the exact χ (2^{32}). Nevertheless, despite not finding the stacked stripe pattern we do find a clear Néel AF pattern for $J_1 > J_2$ and vanishing long-range correlators around $J_1 = 2J_2$. Let us first look at the maximum distance spin-spin correlators before we continue with the higher order correlators from equations 5.19 and 5.15.

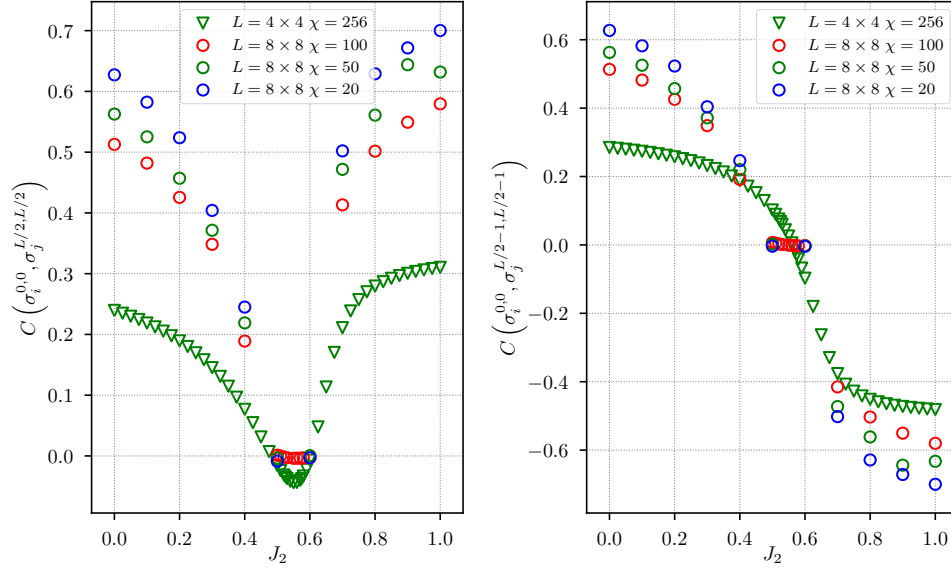


Figure 6.24: Left: $C(L/2, L/2)$ for the 4×4 and 8×8 lattice. Right: $C(L/2 - 1, L/2 - 1)$ for the 4×4 and 8×8 lattice.

In the left plot of figure 6.24 the maximum distance spin-spin correlator is shown and in the right plot of figure 6.24 its adjusted form is shown. With *adjusted* the correlator with maximum distance in the x direction and maximum distance -1 for the y direction as this correlator is expected to have positive sign in the Néel AF and negative sign in the stripe AF. The left plot shows decreasing maximum distance correlators as J_2 increases towards $J_1 = 2J_2$ for both the 4×4 and the 8×8 lattice. For the 8×8 lattice, however, we do observe a vanishing correlator around $J_1 = 2J_2$ and a smoother curve as χ increases. Looking at the right plot we again observe that the correlators for the 8×8 lattice vanish around the maximally frustrated point whereas for the 4×4 lattice they merely switch in sign as the system transitions from a Néel AF to a stripe AF phase. Let us now continue to the higher order correlators to attempt to identify the phase around $J_1 = 2J_2$.

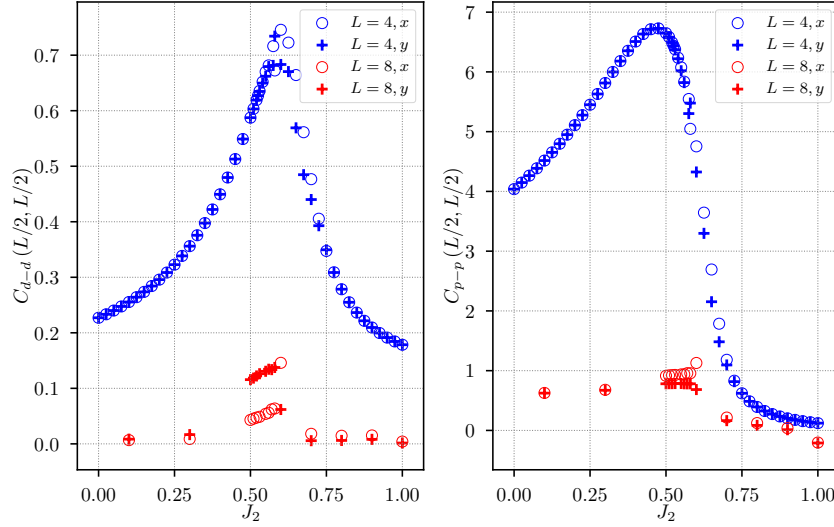


Figure 6.25: Left: Dimer-dimer correlator defined in equation 5.15. Right: Plaquette-plaquette correlator defined in equation 5.19. Both are computed for system sizes of linear size $L = 4$ and $L = 8$, with $\chi = 256$ and $\chi = 100$ respectively

In the left plot of figure 6.25 the dimer-dimer correlators at maximum distance are shown and in the right plot the plaquette-plaquette correlators at maximum distance are shown for both the 4×4 and 8×8 lattice. As observed, the dimer-dimer correlator for the 4×4 lattice increases towards $J_2/J_1 = 0.5$ showing a strong dimer-dimer order but reaches its maximum near $J_2/J_1 = 0.6$ whereas the plaquette-plaquette correlator reaches its maximum near $J_2/J_1 = 0.5$ before it rapidly decreases as the system enters the stripe AF phase, which is not surprising since the stripe AF phase does not allow for plaquette orderings whereas the Néel AF phase does allow for such orderings. These observations, combined with the previous observations of the spin-spin correlator suggest a VBC order around $J_1 = 2J_2$ for the 4×4 lattice. Continuing with the 8×8 lattice, we observe results similar to those of the 4×4 lattice for both type of correlators albeit smaller, suggesting that the presumed VBC order is most likely caused by finite size effects. Interesting is the relatively large difference between the dimer-dimer correlators in the x direction and those in the y direction, however, as mentioned in

section 6.4.1 the TTN for the 8×8 lattice has 4 layers meaning that the lowest tensors cover rectangular sections of the lattice which together with the usage of translational invariance can cause preferred dimer orderings on these sections as is observed in the results above. The results for the plaquette-plaquette correlators of the 8×8 lattice do not show such large differences.

Although the results for $\chi < 100$ are absent, we expect them to yield correlators with higher values as they did for the spin-spin correlators.

Chapter 7

Conclusion & outlook

Gathering the results for the TFI the TTN ansatz does seem to have reasonably well approximations for the ground-state energies compared to the ED results although a relatively high bond-dimension is required. In addition the usage of a finite bond-dimension can lead to poor convergence and the system ending up in some state that is not the ground-state which is illustrated by the figures showing the magnetizations for the TFI models in 1D and 2D. Despite this inaccuracy the correlators do not seem to suffer from the finite χ and are still able to reproduce results similar to the exact diagonalization results. A continuation of this study on the TTN ansatz could include gathering results for larger lattices and determine the entropy scaling. The latter has actually been done [47] and it was shown to not obey the entropic area law.

When evaluating the results for the $J_1 - J_2$ Heisenberg model, we again obtain reasonably good approximations within the exact regime (where comparison to ED results is available/can be performed). We are able to distinguish between Néel AF phase and the stripe AF phase. In between these phases, the transition is centred around $J_2/J_1 = 0.5$, and we observe a steep decrease in the gap between the ground -and the first excited-state around $J_2 = 0.6$ where the intermediate phase transitions to a stripe AF phase. In terms of the dimer-dimer and plaquette-plaquette correlators we find both a strong dimer and plaquette order for this intermediate phase within $0.4 < J_2 < 0.6$ of which the former even persists towards the stripe phase. This raises the question whether this VBS order with possible VBC order persists in the thermodynamic limit, which requires results for increasingly larger lattices to both determine the order and determine whether the gap closes. Another interesting continuation would be to include symmetric

tensors that preserve global symmetries such as $\mathcal{U}(1)$, \mathbb{Z}_2 , and $SU(2)$ in the TTN ansatz [42], and compare to studies on the $J_1 - J_2$ model that also include such symmetries.

As mentioned before a finite size scaling study must be performed for both models to estimate the behaviour in the thermodynamic limit. Since the TTN requires large values for the bond-dimension it will be computationally expensive suggesting that for large lattices (or chains) another tensor network ansatz is probably preferred.

Chapter 8

Acknowledgements

Firstly I would like to thank my supervisor, Dr Philippe Corboz for his unending patience and help during times it was needed and I would like to thank Schelto Crone for the talks we have had and giving me access to the workstation where most of the simulations were done. Secondly I would like to thank Ismani, Kriek, Sebastiaan, Willem, Bram, Thomas, and Sjoerd for the talks, advice, and discussions during the last couple of months writing my thesis. Lastly I would like to thank my mother for the support and Ricardo[†] for having the privilege of knowing him.

Appendix A

Details about Code

A.1 Introduction

The entire project is done in *Python 3.8.1* and can be found on the following git (where I have copied my code from my private repository):

<https://github.com/10434542/TreeTensorNetwork.git> and heavily relies on the package *optimal-einsum* [9] which aims to reduce overall contraction costs by introducing intermediate contractions. The code can be run on the GPU using *PyTorch* and on the CPU using *NumPy*. It is not completely optimized yet, but that is a work in progress.

Bibliography

- [1] P. W. Anderson. The resonating valence bond state in La_2CuO_4 and superconductivity. *science*, 235(4793):1196–1198, 1987.
- [2] N. Bao, C. Cao, S. M. Carroll, and A. Chatwin-Davies. de sitter space as a tensor network: Cosmic no-hair, complementarity, and complexity. *Physical Review D*, 96(12):123536, 2017.
- [3] C. Beny. Causal structure of the entanglement renormalization ansatz. *New Journal of Physics*, 15(2):023020, 2013.
- [4] L. Bombelli, R. K. Koul, J. Lee, and R. D. Sorkin. Quantum source of entropy for black holes. *Phys. Rev. D*, 34:373–383, Jul 1986.
- [5] T. W. Burkhardt and J. M. J. van Leeuwen. *Progress and Problems in Real-Space Renormalization*, pages 1–31. Springer Berlin Heidelberg, Berlin, Heidelberg, 1982.
- [6] G. K.-L. Chan, J. J. Dorando, D. Ghosh, J. Hachmann, E. Neuscamman, H. Wang, and T. Yanai. An introduction to the density matrix renormalization group ansatz in quantum chemistry. In *Frontiers in quantum systems in chemistry and physics*, pages 49–65. Springer, 2008.
- [7] J. Chen, S. Cheng, H. Xie, L. Wang, and T. Xiang. Equivalence of restricted boltzmann machines and tensor network states. *Physical Review B*, 97(8):085104, 2018.
- [8] B. Czech, L. Lamprou, S. McCandlish, and J. Sully. Tensor networks from kinematic space. *Journal of High Energy Physics*, 2016(7):100, 2016.
- [9] S. J. G. Daniel G. A. opt-einsum - a python package for optimizing contraction order for einsum-like expressions. *Journal of Open Source Software*, 3(26), page 753, June 2018.

- [10] G. Evenbly and G. Vidal. Algorithms for entanglement renormalization. *Phys. Rev. B*, 79:144108, Apr 2009.
- [11] G. Evenbly and G. Vidal. Algorithms for entanglement renormalization. *Physical Review B*, 79(14):144108, 2009.
- [12] G. Evenbly and G. Vidal. Entanglement renormalization in two spatial dimensions. *Phys. Rev. Lett.*, 102:180406, May 2009.
- [13] G. Evenbly and G. Vidal. Tensor network renormalization. *Phys. Rev. Lett.*, 115:180405, Oct 2015.
- [14] G. Evenbly and G. Vidal. Tensor network renormalization. *Physical review letters*, 115(18):180405, 2015.
- [15] M. E. Fisher. Renormalization group theory: Its basis and formulation in statistical physics. *Rev. Mod. Phys.*, 70:653–681, Apr 1998.
- [16] J.-B. Fouet, M. Mambrini, P. Sindzingre, and C. Lhuillier. Planar pyrochlore: A valence-bond crystal. *Physical Review B*, 67(5):054411, 2003.
- [17] I. Glasser, N. Pancotti, and J. I. Cirac. Supervised learning with generalized tensor networks. *arXiv preprint arXiv:1806.05964*, 2018.
- [18] S.-S. Gong, W. Zhu, D. Sheng, O. I. Motrunich, and M. P. Fisher. Plaquette ordered phase and quantum phase diagram in the spin-1 $2j_1 - j_2$ square heisenberg model. *Physical review letters*, 113(2):027201, 2014.
- [19] Z.-C. Gu and X.-G. Wen. Tensor-entanglement-filtering renormalization approach and symmetry-protected topological order. *Physical Review B*, 80(15):155131, 2009.
- [20] J. Haegeman, T. J. Osborne, H. Verschelde, and F. Verstraete. Entanglement renormalization for quantum fields in real space. *Physical review letters*, 110(10):100402, 2013.
- [21] M. B. Hastings. An area law for one-dimensional quantum systems. *Journal of Statistical Mechanics: Theory and Experiment*, 2007(08):P08024–P08024, aug 2007.
- [22] W.-J. Hu, F. Becca, A. Parola, and S. Sorella. Direct evidence for a gapless Z_2 spin liquid by frustrating néel antiferromagnetism. *Phys. Rev. B*, 88:060402, Aug 2013.

- [23] H.-C. Jiang, H. Yao, and L. Balents. Spin liquid ground state of the spin-1 2 square j 1-j 2 heisenberg model. *Physical Review B*, 86(2):024424, 2012.
- [24] L. P. Kadanoff. Scaling laws for ising models near T_c . *Physics Physique Fizika*, 2:263–272, Jun 1966.
- [25] L. P. Kadanoff. Variational principles and approximate renormalization group calculations. *Physical Review Letters*, 34(16):1005, 1975.
- [26] L. P. Kadanoff, W. GÖTZE, D. HAMBLÉN, R. HECHT, E. A. S. LEWIS, V. V. PALCIAUSKAS, M. RAYL, J. SWIFT, D. ASPNES, and J. KANE. Static phenomena near critical points: Theory and experiment. *Rev. Mod. Phys.*, 39:395–431, Apr 1967.
- [27] C. Krumnow, L. Veis, Ö. Legeza, and J. Eisert. Fermionic orbital optimization in tensor network states. *Physical review letters*, 117(21):210402, 2016.
- [28] C. Lacroix, P. Mendels, and F. Mila. *Introduction to frustrated magnetism: materials, experiments, theory*, volume 164. Springer Science & Business Media, 2011.
- [29] P. A. Lee, N. Nagaosa, and X.-G. Wen. Doping a mott insulator: Physics of high-temperature superconductivity. *Rev. Mod. Phys.*, 78:17–85, Jan 2006.
- [30] M. Levin and C. P. Nave. Tensor renormalization group approach to two-dimensional classical lattice models. *Physical review letters*, 99(12):120601, 2007.
- [31] Y. Levine, O. Sharir, N. Cohen, and A. Shashua. Quantum entanglement in deep learning architectures. *Physical review letters*, 122(6):065301, 2019.
- [32] Y. Levine, D. Yakira, N. Cohen, and A. Shashua. Deep learning and quantum entanglement: Fundamental connections with implications to network design. *arXiv preprint arXiv:1704.01552*, 2017.
- [33] W.-Y. Liu, S. Dong, C. Wang, Y. Han, H. An, G.-C. Guo, and L. He. Gapless spin liquid ground state of the spin- $\frac{1}{2}$ $J_1 - J_2$ heisenberg model on square lattices. *Phys. Rev. B*, 98:241109, Dec 2018.

- [34] M. Mambrini, A. Läuchli, D. Poilblanc, and F. Mila. Plaquette valence-bond crystal in the frustrated heisenberg quantum antiferromagnet on the square lattice. *Physical Review B*, 74(14):144422, 2006.
- [35] E. Miles Stoudenmire and D. J. Schwab. Supervised learning with quantum-inspired tensor networks. *arXiv preprint arXiv:1605.05775*, 2016.
- [36] A. Milsted and G. Vidal. Geometric interpretation of the multi-scale entanglement renormalization ansatz. *arXiv preprint arXiv:1812.00529*, 2018.
- [37] V. Murg, F. Verstraete, and J. I. Cirac. Exploring frustrated spin systems using projected entangled pair states. *Phys. Rev. B*, 79:195119, May 2009.
- [38] T. Nishino and K. Okunishi. Corner transfer matrix renormalization group method. *Journal of the Physical Society of Japan*, 65(4):891–894, 1996.
- [39] S. Östlund and S. Rommer. Thermodynamic limit of density matrix renormalization. *Phys. Rev. Lett.*, 75:3537–3540, Nov 1995.
- [40] H. Rieger and N. Kawashima. Application of a continuous time cluster algorithm to the two-dimensional random quantum ising ferromagnet. *The European Physical Journal B - Condensed Matter and Complex Systems*, 9(2):233–236, May 1999.
- [41] H. Schulz, T. Ziman, and D. Poilblanc. Magnetic order and disorder in the frustrated quantum heisenberg antiferromagnet in two dimensions. *Journal de Physique I*, 6(5):675–703, 1996.
- [42] S. Singh, R. N. Pfeifer, and G. Vidal. Tensor network decompositions in the presence of a global symmetry. *Physical Review A*, 82(5):050301, 2010.
- [43] M. Srednicki. Entropy and area. *Phys. Rev. Lett.*, 71:666–669, Aug 1993.
- [44] S. Suzuki, J.-i. Inoue, and B. K. Chakrabarti. *Quantum Ising phases and transitions in transverse Ising models; 2nd ed.* Lecture notes in physics. Springer, Berlin, 2013.

- [45] B. Swingle. Entanglement renormalization and holography. *Physical Review D*, 86(6):065007, 2012.
- [46] S. Szalay, M. Pfeffer, V. Murg, G. Barcza, F. Verstraete, R. Schneider, and Ö. Legeza. Tensor product methods and entanglement optimization for ab initio quantum chemistry. *International Journal of Quantum Chemistry*, 115(19):1342–1391, 2015.
- [47] L. Tagliacozzo, G. Evenbly, and G. Vidal. Simulation of two-dimensional quantum systems using a tree tensor network that exploits the entropic area law. *Physical Review B*, 80(23):235127, 2009.
- [48] F. Verstraete and J. I. Cirac. Continuous matrix product states for quantum fields. *Physical review letters*, 104(19):190405, 2010.
- [49] L. Wang, Z.-C. Gu, F. Verstraete, and X.-G. Wen. Tensor-product state approach to spin- $\frac{1}{2}$ square J_1-J_2 antiferromagnetic heisenberg model: Evidence for deconfined quantum criticality. *Phys. Rev. B*, 94:075143, Aug 2016.
- [50] L. Wang and A. W. Sandvik. Critical level crossings and gapless spin liquid in the square-lattice spin-1/2 J_1-J_2 heisenberg antiferromagnet. *Phys. Rev. Lett.*, 121:107202, Sep 2018.
- [51] Y.-C. Wang, X.-F. Zhang, F. Pollmann, M. Cheng, Z. Y. Meng, et al. Quantum spin liquid with even ising gauge field structure on kagome lattice. *Physical review letters*, 121(5):057202, 2018.
- [52] X.-G. Wen. Vacuum degeneracy of chiral spin states in compactified space. *Physical Review B*, 40(10):7387, 1989.
- [53] X.-G. Wen. Mean-field theory of spin-liquid states with finite energy gap and topological orders. *Physical Review B*, 44(6):2664, 1991.
- [54] X.-G. Wen and Q. Niu. Ground-state degeneracy of the fractional quantum hall states in the presence of a random potential and on high-genus riemann surfaces. *Physical Review B*, 41(13):9377, 1990.
- [55] S. R. White. Density matrix formulation for quantum renormalization groups. *Phys. Rev. Lett.*, 69:2863–2866, Nov 1992.
- [56] S. R. White and R. L. Martin. Ab initio quantum chemistry using the density matrix renormalization group. *The Journal of chemical physics*, 110(9):4127–4130, 1999.

- [57] A. Wietek and A. M. Läuchli. Chiral spin liquid and quantum criticality in extended $s = \frac{1}{2}$ heisenberg models on the triangular lattice. *Phys. Rev. B*, 95:035141, Jan 2017.
- [58] K. G. Wilson. The renormalization group: Critical phenomena and the kondo problem. *Rev. Mod. Phys.*, 47:773–840, Oct 1975.
- [59] J.-F. Yu and Y.-J. Kao. Spin-1 2 j 1-j 2 heisenberg antiferromagnet on a square lattice: A plaquette renormalized tensor network study. *Physical Review B*, 85(9):094407, 2012.